Spin injection and spin accumulation in all-metal mesoscopic spin valves

F. J. Jedema,* M. S. Nijboer, A. T. Filip,† and B. J. van Wees
Department of Applied Physics and Materials Science Center, University of Groningen, Nijenborgh 4, 9747 AG Groningen, The Netherlands

(Received 25 July 2002; published 28 February 2003)

We study the electrical injection and detection of spin accumulation in lateral ferromagnetic-metal–nonmagnetic-metal–ferromagnetic-metal (F/N/F) spin valve devices with transparent interfaces. Different ferromagnetic metals, Permalloy (Py), cobalt (Co), and nickel (Ni), are used as electrical spin injectors and detectors. For the nonmagnetic metal both aluminum (Al) and copper (Cu) are used. Our multiterminal geometry allows us to experimentally separate the spin valve effect from other magnetoresistance signals such as the anisotropic magnetoresistance and Hall effects. In a ''nonlocal'' spin valve measurement we are able to completely isolate the spin valve signal and observe clear spin accumulation signals at $T=4.2$ K as well as at room temperature (RT). For aluminum we obtain spin relaxation lengths (λ_{sf}) of 1.2 μm and 600 nm at $T=4.2$ K and RT, respectively, whereas for copper we obtain 1.0 μm and 350 nm. At RT these spin relaxation lengths are within a factor of 2 of the maximal obtainable spin relaxation length, being limited by electron-phonon scattering. The spin relaxation times τ_{sf} in the Al and Cu thin films are compared with theory and results obtained from giant magnetoresistance (GMR), conduction electron spin resonance, antiweak localization, and superconducting tunneling experiments. The magnitudes of the spin valve signals generated by the Py and Co electrodes are compared to the results obtained from GMR experiments. For the Ni electrodes no spin signal could be observed beyond experimental accuracy.

DOI: 10.1103/PhysRevB.67.085319 PACS number(s): 72.25.Ba, 72.25.Hg, 72.25.Mk, 72.25.Rb

I. INTRODUCTION

Spintronics is a rapidly emerging field in which one tries to study or make explicit use of the spin degree of freedom of the electron.[1–3] So far, the most well-known examples of spintronics are the giant magnetoresistance (GMR) of metallic multilayers[4–6] and tunneling magnetoresistance (TMR) of magnetic tunnel junctions.[7,8] Injection of hot electrons ≈ 1 eV above the Fermi energy (E_F) in Co/Cu (multi)layers have shown a significant spin filtering effect, enabling transistor functionality and ballistic electron magnetic microscopy.[9,10] Recent experiments have shown the ability of spin-polarized currents to induce a (local) magnetization reversal in thin ferromagnetic wires and Co/Cu multilayer pillars.[11–15] A new direction is emerging, where one actually wants to inject spin currents, transfer and manipulate the spin information at the Fermi energy, and detect the resulting spin polarization in nonmagnetic metals and semiconductors.[16] Because of the spin-orbit interaction, the electron spin can be flipped and consequently a spin-polarized current will have a finite lifetime. For this reason it is necessary to study spin transport in systems, where the ''time of flight'' of the electrons between the injector and detector is shorter than the spin relaxation time. A first successful attempt to electrically inject and detect spins in metals dates back to 1985 when Johnson and Silsbee demonstrated spin accumulation in a single-crystal aluminum bar up to temperatures of 77 K.[17,18] In their pioneering experiments they were able to observe spin precession of the induced nonequilibrium magnetization, made possible by the long spin relaxation lengths $\lambda_{sf} > 50$ μm. In (diffusive) thin metallic films, however, the spin relaxation length corresponds to typical length scales of 1 μm. We use a lateral mesosopic spin valve to access and probe this length scale.[19–22] We note that a similar experiment using planar spin valves has been reported in Ref. 23.

In Sec. II a review of the basic model for spin transport in the diffusive transport regime is given, whereas in Sec. III this model is applied to our multiterminal device geometry. A multiterminal resistor model of spin injection and detection is presented in Sec. IV in order to elucidate the principles behind the reduction of the polarization of the spin current at a transparent F/N interface, also referred to as ''conductivity mismatch.''[24] The sample fabrication process and measurement geometry are described in Sec. V. Spin accumulation measurements in a ''conventional'' and ''nonlocal'' geometry for Py/Cu/Py and Py/Al/Py spin valves will be presented in Sec. VI and Sec. VII, whereas spin accumulation measurements on Co/Cu/Co and Ni/Cu/Ni spin valves will be presented in Sec. VIII. In Sec. IX the obtained results of Secs. VI, VII, and VIII are analyzed using the model for spin transport in the diffusive regime and the results are compared to current perpendicular-to-plane- (CPP-) GMR, conduction electron spin resonance (CESR), antiweak localization, and superconducting tunneling experiments.

II. THEORY OF SPIN INJECTION AND ACCUMULATION

In general, electron transport through a diffusive channel is a result of a difference in the electrochemical potential of two connected electron reservoirs.[25] An electron reservoir is an electron bath in full thermal equilibrium. In the absence of a magnetic field the electrochemical potential (μ) is obtained by adding the chemical energy (μ_{ch}) and the potential energy:

$$\mu = \mu_{ch} - eV. \tag{1}$$

Here e denotes the absolute value of the electron charge and V is the electric potential of the reservoir. The chemical po-

tential μ_{ch} is by definition the energy needed to add one electron to the system, usually set to zero at the Fermi energy (this convention is adopted throughout this text), and accounts for the kinetic energy of the electrons. In the linear response regime, i.e., for small deviations from equilibrium ($|eV|<kT$), the chemical potential equals the excess electron density n divided by the density of states (N) at the Fermi energy, $\mu_{ch}=n/N(E_F)$.

From Eq. (1) it is clear that a gradient of μ, the driving force of electron transport, can result from either a spatial varying electron density ∇n or an electric field $\mathbf{E}=-\nabla V$. Since μ fully characterizes the reservoir, one is free to describe transport either in terms of diffusion ($\mathbf{E}=0$, $\nabla n\neq 0$) or in terms of electron drift ($\mathbf{E}\neq 0$, $\nabla n=0$). In the drift picture the whole Fermi sea has to be taken into account and consequently one has to maintain a constant electron density everywhere by imposing $\nabla n=0$. We use the diffusive picture where only the energy range $\Delta\mu$, the difference in the electrochemical potential between the two reservoirs, is important to describe transport. Both approaches (drift and diffusion) are equivalent in the linear regime and are related to each other via the Einstein relation

$$\sigma=e^2N(E_F)D, \tag{2}$$

where σ is the conductivity and D the diffusion constant.

We focus on the diffusive transport regime, which applies when the mean free path l_e is shorter than the device dimensions. The description of electrical transport in a ferromagnetic metal in terms of a two-current (spin-up and spin-down) model dates back to Mott.[26] This idea was followed by Campbell and co-workers to describe the transport properties of Ni-, Fe-, and Co-based alloys.[27–30] van Son *et al.*[31] have extended the model to describe transport through F/N interfaces. A firm theoretical underpinning, based on the Boltzmann transport equation, has been given by Valet and Fert.[32] They have applied the model to describe the effects of spin accumulation and spin-dependent scattering on the CPP-GMR effect in magnetic multilayers. This standard model allows for a detailed quantitative analysis of the experimental results.

An alternative model, based on thermodynamic considerations, has been put forward and applied by Johnson and Silsbee (JS).[33] In principle, both models describe the same physics and should therefore be equivalent. However, the JS model has a drawback in that it does not allow a direct calculation of the spin polarization of the current (η in Refs. 17,18, and 33–35), whereas in the standard model all measurable quantities can be directly related to the parameters of the experimental system.[32,36,37]

The transport in a ferromagnet is described by spin-dependent conductivities

$$\sigma_\uparrow=N_\uparrow e^2D_\uparrow, \text{ with } D_\uparrow=\frac{1}{3}v_{F\uparrow}l_{e\uparrow}, \tag{3}$$

$$\sigma_\downarrow=N_\downarrow e^2D_\downarrow, \text{ with } D_\downarrow=\frac{1}{3}v_{F\downarrow}l_{e\downarrow}, \tag{4}$$

where $N_{\uparrow,\downarrow}$ denotes the spin-dependent density of states (DOS) at the Fermi energy and $D_{\uparrow,\downarrow}$ the spin-dependent diffusion constants, expressed in the spin dependent Fermi velocities $v_{F\uparrow,\downarrow}$ and electron mean free paths $l_{e\uparrow,\downarrow}$. Throughout this paper our notation is $\uparrow$ for the majority spin direction and $\downarrow$ for the minority spin direction. Note that the spin dependence of the conductivities is determined by *both* the density of states and diffusion constants. This should be contrasted with magnetic F/I/F or F/I/N tunnel junctions, where the spin polarization of the tunneling electrons is determined (to first order) by the spin-dependent (local) DOS.[7,38,39] Also in a typical ferromagnet several bands (which generally have different spin-dependent densities of states and Fermi velocities) contribute to the transport. Provided that the elastic scattering time and the interband scattering times are shorter than the spin flip times (which is usually the case), the transport can still be described in terms of well-defined spin-up and spin-down conductivities. It should, however, be noted that in particular ferromagnets (e.g., Permalloy[40–42]) the spin flip times may become comparable to the momentum scattering time. In this case an (additional) spin-mixing resistance arises,[4,29,43] which we will not discuss further here.

Because the spin-up and spin-down conductivities are different, the current in the bulk ferromagnet will be distributed accordingly over the two spin channels:

$$j_\uparrow=\frac{\sigma_\uparrow}{e}\frac{\partial\mu_\uparrow}{\partial x} \tag{5}$$

$$j_\downarrow=\frac{\sigma_\downarrow}{e}\frac{\partial\mu_\downarrow}{\partial x}, \tag{6}$$

where $j_{\uparrow\downarrow}$ are the spin-up and spin-down current densities. According to Eqs. (5) and (6) the current flowing in a bulk ferromagnet is spin polarized, with a polarization given by

$$\alpha_F=\frac{\sigma_\uparrow-\sigma_\downarrow}{\sigma_\uparrow+\sigma_\downarrow}. \tag{7}$$

The next step is the introduction of spin flip processes, described by a spin flip time $\tau_{\uparrow\downarrow}$ for the average time to flip an up spin to a down spin and $\tau_{\downarrow\uparrow}$ for the reverse process. The detailed balance principle imposes that $N_\uparrow/\tau_{\uparrow\downarrow}=N_\downarrow/\tau_{\downarrow\uparrow}$, so that in equilibrium no net spin scattering takes place. As pointed out already, usually these spin flip times are larger than the momentum scattering time $\tau_e=l_e/v_F$. The transport can then be described in terms of the parallel diffusion of the two spin species, where the densities are controlled by spin flip processes.

The effect of the spin flip processes can now be described by the following equation (assuming diffusion in one dimension only):[37]

$$D\frac{\partial^2(\mu_\uparrow-\mu_\downarrow)}{\partial x^2}=\frac{(\mu_\uparrow-\mu_\downarrow)}{\tau_{sf}}, \tag{8}$$

where $D=D_\uparrow D_\downarrow(N_\uparrow+N_\downarrow)/(N_\uparrow D_\uparrow+N_\downarrow D_\downarrow)$ is the spin-averaged diffusion constant, and the spin relaxation time τ_{sf} is given by $1/\tau_{sf}=1/\tau_{\uparrow\downarrow}+1/\tau_{\downarrow\uparrow}$. We note that τ_{sf} represents

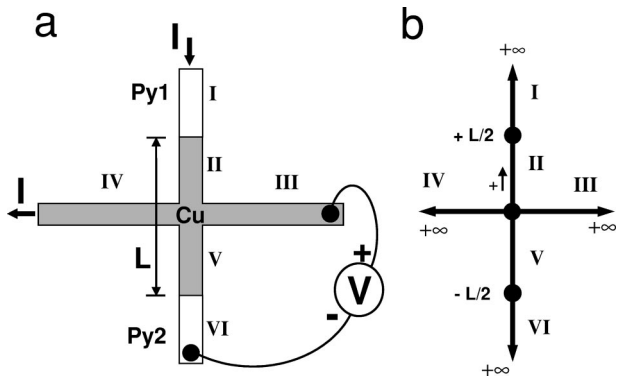

FIG. 1. (a) Schematic representation of the multiterminal spin valve device. Regions I and VI denote the injecting (F_1) and detecting (F_2) ferromagnetic contacts, whereas regions II–V denote the four arms of a normal metal cross (N) placed in between the two ferromagnets. A spin-polarized current is injected from region I into region II and extracted at region IV. (b) Diagram of the electrochemical potential solutions [Eqs. (9) and (10)] in each of the six regions of the multiterminal spin valve. The nodes represent the origins of the coordinate axis in the six regions; the arrows indicate the (chosen) direction of the positive x coordinate. Regions II and V have a finite length of half the Py electrode spacing L. The other regions are semi-infinite.

the time scale over which the nonequilibrium spin accumulation ($\mu_\uparrow - \mu_\downarrow$) decays and therefore is equal to the spin lattice relaxation time T_1 used in the Bloch equations: $\tau_{sf} = T_1$.[18,44] Using the requirement of current conservation, the general solution of Eq. (8) for a uniform ferromagnet or nonmagnetic wire is now given by

$$\mu_\uparrow = a + bx + \frac{c}{\sigma_\uparrow}\exp(-x/\lambda_{sf}) + \frac{d}{\sigma_\uparrow}\exp(x/\lambda_{sf}), \quad (9)$$

$$\mu_\downarrow = a + bx - \frac{c}{\sigma_\downarrow}\exp(-x/\lambda_{sf}) - \frac{d}{\sigma_\downarrow}\exp(x/\lambda_{sf}), \quad (10)$$

where we have introduced the spin relaxation length $\lambda_{sf} = \sqrt{D\tau_{sf}}$. The coefficients a, b, c, and d are determined by the boundary conditions imposed at the junctions where the wires are coupled to other wires. In the absence of an interface resistance and spin flip scattering at the interfaces, the boundary conditions are (1) continuity of $\mu_\uparrow$ $\mu_\downarrow$ at the interface, and (2) conservation of spin-up and spin-down currents $j_\uparrow$, $j_\downarrow$ across the interface.

III. SPIN ACCUMULATION IN MULTITERMINAL SPIN VALVE STRUCTURES

We will now apply the model of spin injection to a multiterminal geometry, which reflects our measurement and device geometry; see Figs. 1(a) and 3(c).

In our (one-dimensional) geometry we can identify six different regions for which Eqs. (9) and (10) have to be solved according to their boundary conditions at the interface. The geometry is schematically shown in Fig. 1(b), where the six different regions are marked with roman letters I–VI. According to Eq. (9) the equations for the spin-up electrochemical potentials in these regions, assuming parallel magnetization of the ferromagnetic regions, read

$$\mu_\uparrow = A - \frac{je}{\sigma_F}x + \frac{2C}{\sigma_F(1+\alpha_F)}\exp(-x/\lambda_F), \quad \text{(I)}$$

$$\mu_\uparrow = \frac{-je}{\sigma_N}x + \frac{2E}{\sigma_N}\exp(-x/\lambda_N) + \frac{2F}{\sigma_N}\exp(x/\lambda_N), \quad \text{(II)}$$

$$\mu_\uparrow = \frac{2G}{\sigma_N}\exp(-x/\lambda_N), \quad \text{(III)}$$

$$\mu_\uparrow = \frac{je}{\sigma_N}x + \frac{2G}{\sigma_N}\exp(-x/\lambda_N), \quad \text{(IV)}$$

$$\mu_\uparrow = \frac{2H}{\sigma_N}\exp(-x/\lambda_N) + \frac{2K}{\sigma_N}\exp(x/\lambda_N), \quad \text{(V)}$$

$$\mu_\uparrow = B + \frac{2D}{\sigma_F(1+\alpha_F)}\exp(-x/\lambda_F), \quad \text{(VI)}$$

where we have written $\sigma_\uparrow = \sigma_F(1+\alpha_F)/2$ and A to K are nine unknown constants. The equations for the spin-down electrochemical potential in the six regions of Fig. 1 can be found by putting a minus sign in front of the constants C, D, E, F, H, K, G, and α_F in Eqs. (I)–(VI). The constant B is the most valuable to extract from this set of equations, for it gives directly the difference between the electrochemical potential measured with a normal metal probe at the center of the nonmagnetic metal cross in Fig. 1(a) and the electrochemical potential measured with a ferromagnetic voltage probe at the F/N interface of regions V and VI. For $\lambda_N \gg L$ i.e. no spin relaxation in the nonmagnetic metal of regions II and V, the ferromagnetic voltage probe effectively probes the electrochemical potential difference between spin-up and spin-down electrons at center of the nonmagnetic metal cross. Solving Eqs. (I)–(VI) by taking the continuity of the spin-up and spin-down electrochemical potentials and the conservation of spin-up and spin-down-currents at the three nodes of Fig. 1(b), one obtains

$$B = -je\frac{\alpha_F^2\frac{\lambda_N}{\sigma_N}e^{-L/2\lambda_N}}{2(M+1)[M\sinh(L/2\lambda_N)+\cosh(L/2\lambda_N)]}, \quad (11)$$

where $M = (\sigma_F\lambda_N/\sigma_N\lambda_F)(1-\alpha_F^2)$ and L is the length of the nonmagnetic metal strip in between the ferromagnetic electrodes. The magnitude of the spin accumulation at the F/N interface of regions V and VI is given by $\mu_\uparrow - \mu_\downarrow = 2B/\alpha_F$.

In the situation where the ferromagnets have an antiparallel magnetization alignment, the constant B of Eq. (11) gets a minus sign in front. Upon changing from parallel to antiparallel magnetization configuration (a spin valve measurement) a difference of $\Delta\mu = 2B$ will be detected in the electrochemical potential between the normal metal (Region III) and ferromagnetic voltage probe (Region VI). This leads to

the definition of the spin-dependent resistance $\Delta R = -2B/ejS$, where S is the cross-sectional area of the nonmagnetic strip:

$$\Delta R = \frac{\alpha_F^2 \frac{\lambda_N}{\sigma_N S} e^{-L/2\lambda_N}}{(M+1)[M \sinh(L/2\lambda_N) + \cosh(L/2\lambda_N)]}. \quad (12)$$

Equation (12) shows that for $\lambda_N \ll L$, the magnitude of the spin signal ΔR will decay exponentially as a function of L. In the opposite limit $\lambda_F \ll L \ll \lambda_N$, the spin signal ΔR has a $1/L$ dependence. In this limit and under the constraint that $ML/2\lambda_N \gg 1$, we can write Eq. (12) as

$$\Delta R = \frac{2\alpha_F^2 \lambda_N^2}{M(M+1)\sigma_N SL}. \quad (13)$$

Subsequently, in the situation where there are no spin flip events in the normal metal ($\lambda_N \to \infty$) we find that we can write Eq. (13) in an even more simple form

$$\Delta R = \frac{2\alpha_F^2 \lambda_F^2/\sigma_F^2}{(1-\alpha_F^2)^2 SL/\sigma_N}. \quad (14)$$

The important point to notice is that Eq. (14) clearly shows that even in the situation when there are no spin flip processes in the normal metal, the spin signal ΔR is reduced with increasing L. The reason is that the *spin-dependent* resistance ($\lambda_F/\sigma_F S$) of the injecting and detecting ferromagnets remains constant for the two spin channels, whereas the *spin-independent* resistance ($L/\sigma_N S$) of the nonmagnetic metal in between the two ferromagnets increases linearly with L. In both nonmagnetic metal regions II and V (Fig. 1) the spin currents have to traverse a total resistance path over a length $\lambda_F + L/2$ and therefore the polarization of the current flowing through these regions will decrease linearly with L and hence the spin signal ΔR. Note that in regions V and VI no net current is flowing as the opposite flowing spin-up and spin-down currents are equal in magnitude.

Using Eqs. (5), (6), and (I) we can calculate the current polarization *at the interface* of the current injecting contact, defined as $P = (j_\uparrow^{int} - j_\downarrow^{int})/(j_\uparrow^{int} + j_\downarrow^{int})$. We obtain

$$P = \alpha_F \frac{M e^{L/2\lambda_N} + 2\cosh(L/2\lambda_N)}{2(M+1)[M \sinh(L/2\lambda_N) + \cosh(L/2\lambda_N)]}. \quad (15)$$

In the limit that $L \gg \lambda_N$ we obtain the polarization of the current at a single F/N interface:[31]

$$P = \frac{\alpha_F}{M+1}. \quad (16)$$

Again, Eq. (16) shows a reduction of the polarization of the current at the F/N interface, when the spin-dependent resistance ($\lambda_F/\sigma_F S$) is much smaller that the spin-independent resistance ($\lambda_N/\sigma_N S$) of the nonmagnetic metal. This situation becomes progressively worse for a semiconductor as σ_N is reduced by a factor of 100 or more and has become known as the ''conductivity mismatch.''[24,45]

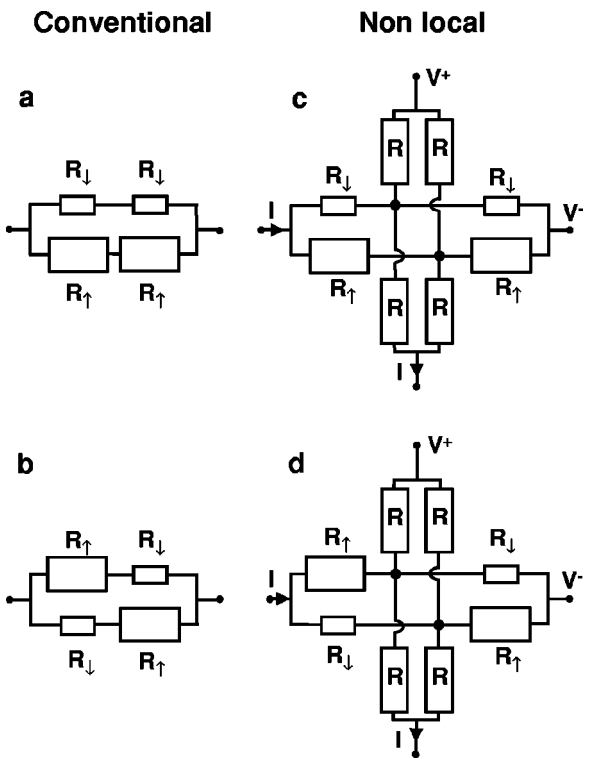

FIG. 2. The equivalent resistor networks of the spin valve device. (a) The conventional spin valve geometries in parallel and (b) in antiparallel configurations. (c) The nonlocal spin valve geometry in parallel and (d) in antiparallel configurations.

Finally we note that the spin signal ΔR^{Conv} can also be calculated for a conventional measurement geometry [see Fig. 3(b)], writing down similar equations and boundary conditions as we have done for the nonlocal geometry [Eqs. (I)–(VI)]. We find

$$\Delta R^{Conv} = 2\Delta R. \quad (17)$$

Equation (17) shows that the magnitude of the spin valve signal measured with a conventional geometry is increased with a factor of 2 as compared to the nonlocal spin valve geometry [see also Ref. 36, Eq. (45)].

IV. RESISTOR MODEL OF MULTITERMINAL SPIN VALVE STRUCTURES

More physical insight can be gained by considering an equivalent resistor network of the spin valve device.[46] In the linear transport regime, where the measured voltages are linear functions of the applied currents, the spin transport for the conventional and nonlocal geometry can be represented by a two-terminal and four-terminal resistor network, respectively. This is shown in Fig. 2 for both parallel and antiparallel configurations of the ferromagnetic electrodes. The resistances $R_\downarrow$ and $R_\uparrow$ represent the resistances of the spin-up and spin-down channels, which consists of the different spin-up and spin-down resistance of the ferromagnetic elec-

trodes ($R^F_\uparrow, R^F_\downarrow$) and the spin-independent resistance R^N of the nonmagnetic wire in between the ferromagnetic electrodes. From resistor model calculations we obtain

$$R_\uparrow = R^F_\uparrow + R^N = \frac{2\lambda_F}{w(1+\alpha_F)} R^F{}_\square + \frac{L}{w} R^N{}_\square, \tag{18}$$

$$R_\downarrow = R^F_\downarrow + R^N = \frac{2\lambda_F}{w(1-\alpha_F)} R^F{}_\square + \frac{L}{w} R^N{}_\square, \tag{19}$$

where $R^F{}_\square = 1/\sigma_F h$ and $R^N{}_\square = 1/\sigma_N h$ are the "square" resistances of the ferromagnet and nonmagnetic metal thin films, and w and h are the width and height of the nonmagnetic metal strip. The resistance $R = (\lambda_N - L/2) 2R^N{}_\square / w$ in Figs. 2(c) and 2(d) represents the resistance for one spin channel in the side arms of the nonmagnetic metal cross over a length $\lambda_N - L/2$, corresponding to regions III and IV of Fig. 1(a).

Provided that $\lambda_N \gg L$ the spin-dependent resistance ΔR^{Conv} between the parallel [Fig. 2(a)] and antiparallel (Fig. 2(b)] resistor networks for the conventional geometry can be calculated. We obtain the familiar expression[4,6]

$$\Delta R^{Conv} = \frac{(R_\downarrow - R_\uparrow)^2}{2(R_\uparrow + R_\downarrow)}. \tag{20}$$

For the nonlocal geometry and under the condition $\lambda_N \gg L$ the spin-dependent resistance ΔR between the parallel [Fig. 2(c)] and antiparallel [Fig. 2(d)] resistor networks can also be calculated. We obtain

$$\Delta R = \frac{(R_\downarrow - R_\uparrow)^2}{4(R_\uparrow + R_\downarrow)}. \tag{21}$$

Equation (21) again shows that the spin signal measured in a nonlocal geometry is reduced by a factor of 2 as compared to a conventional measurement. Provided that $R^F_\uparrow, R^F_\downarrow \ll R^N$ we can use Eqs. (18) and (19) to rewrite Eq. (21) as

$$\Delta R = \frac{2\alpha_F^2 \lambda_F^2 R^F{}_\square{}^2}{(1-\alpha_F^2)^2 L w R^N{}_\square}. \tag{22}$$

Using $S = wh$ and replacing the square resistance by the conductivities, Eq. (22) reduces to Eq. (14). A direct relation can now be obtained between the experimentally measured quantities ΔR, $R^N{}_\square$, $R^F{}_\square$ and the relevant spin-dependent properties of the ferromagnet:

$$R_\downarrow - R_\uparrow = \sqrt{8 \Delta R R^N{}_\square \frac{L}{w}} = \frac{4\alpha_F \lambda_F R^F{}_\square}{(1-\alpha_F^2) w}. \tag{23}$$

Equation (23) shows that the magnitude of the bulk spin-dependent resistance of the ferromagnetic electrode can be determined directly from the observable experimental quantities as the length, width, and square resistance of the nonmagnetic wire and the spin-dependent resistance ΔR.

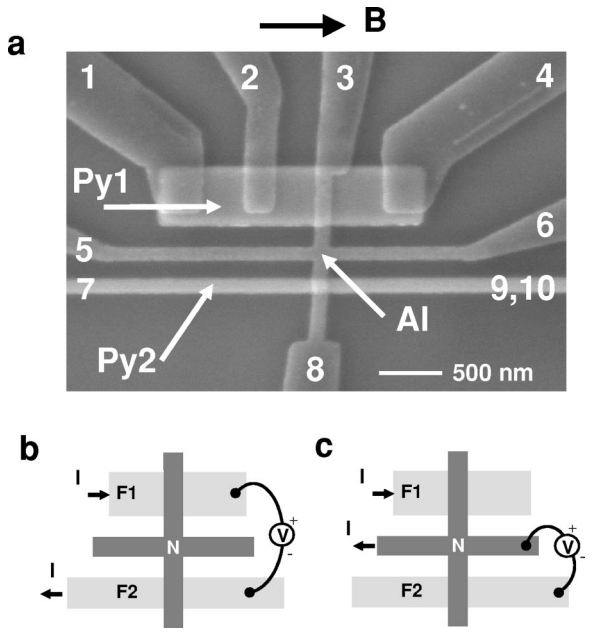

FIG. 3. (a) Scanning electron microscope (SEM) picture of the lateral mesoscopic spin valve device with a ferromagnetic electrode spacing $L = 500$ nm. The two horizontal strips are the ferromagnetic electrodes F1 (Py1) and F2 (Py2). Their sizes are $2 \times 0.5\ \mu m^2$ and $14 \times 0.15\ \mu m^2$, respectively. An aluminum (Al) cross is placed in between the Py electrodes, which vertical arms lay on top of the Py electrodes. A total of ten contacts (not all visible) are connected to the device. (b) The conventional measurement geometry and (c) the nonlocal measurement geometry. The black arrow indicates the direction of the applied magnetic field **B** in the measurements.

V. SAMPLE FABRICATION AND MEASUREMENT GEOMETRY

We use Permalloy $Ni_{80}Fe_{20}$ (Py), cobalt (Co), and nickel (Ni) electrodes to drive a spin-polarized current into copper (Cu) or (Al) crossed strips. Different aspect ratios of the rectangular ferromagnetic injector (F1) and detector strips (F2) result in different switching fields of the magnetization reversal process, allowing control over the relative magnetization configuration of F1 and F2 (parallel and antiparallel) by applying a magnetic field parallel to the long axis of the ferromagnetic electrodes.[47–49] Two sets [F1,F2] of different sizes are used in the experiments. One set has dimensions of $2 \times 0.8\ \mu m^2$ (F1) and $14 \times 0.5\ \mu m^2$ (F2), whereas the other set has dimensions of $2 \times 0.5\ \mu m^2$ (F1) and $14 \times 0.15\ \mu m^2$ (F2). An example of a typical device is shown in Fig. 3.

The devices are fabricated in two steps by means of conventional *e*-beam lithography (EBL) with PMMA resist and liftoff technique. To avoid magnetic fringe fields, the ferromagnetic electrodes are deposited first on a thermally oxidized silicon substrate. The 40-nm-thick Py electrodes are sputter deposited on a 2-nm tantalum (Ta) adhesion layer. The base pressure of the sputter system at IMEC (Belgium) was 2×10^{-8} mbar vacuum, whereas the background Ar pressure during sputtering was 1 mbar. A small **B** field of 3 mT along the long axis of the Py electrodes was applied during growth. The conductivity of the Py film was deter-

mined to be $\sigma_{Py}=6.6\times10^{6}\ \Omega^{-1}\,\mathrm{m}^{-1}$ and $\sigma_{Py}=1.2\times10^{7}\ \Omega^{-1}\,\mathrm{m}^{-1}$ at room temperature (RT) and 4.2 K, respectively. The 40-nm-thick Co (99.95% pure) and 30-nm-thick Ni (99.98% pure) electrodes were deposited by *e*-gun evaporation in a 1×10^{-6} mbar vacuum (base pressure 2×10^{-7} mbar). The conductivities of the Co and Ni films were determined to be $\sigma_{Co}=4.2\times10^{6}\ \Omega^{-1}\,\mathrm{m}^{-1}$ and $\sigma_{Ni}=7.6\times10^{6}\ \Omega^{-1}\,\mathrm{m}^{-1}$ at RT, whereas at 4.2 K they were $\sigma_{Co}=7.3\times10^{6}\ \Omega^{-1}\,\mathrm{m}^{-1}$ and $\sigma_{Ni}=1.6\times10^{7}\ \Omega^{-1}\,\mathrm{m}^{-1}$. In the second EBL fabrication step, 50-nm-thick crossed Cu (99.99% pure) or Al (99.999% pure) strips were deposited by *e*-gun evaporation in a 1×10^{-8} mbar vacuum (base pressure 2×10^{-9} mbar). Prior to the Cu or Al deposition, a few nm of Py, Co, or Ni material was removed from the ferromagnetic electrodes by Kaufmann sputtering at 500 V for 30 sec in a 2×10^{-4} mbar Ar pressure, thereby removing the oxide to ensure transparent contacts. The time in between the Kaufmann sputtering and Cu or Al deposition was about 3 min. The conductivities of the Cu and Al films were determined to be $\sigma_{Cu}=3.5\times10^{7}\ \Omega^{-1}\,\mathrm{m}^{-1}$ and $\sigma_{Al}=3.1\times10^{7}\ \Omega^{-1}\,\mathrm{m}^{-1}$ at RT, whereas at 4.2 K they were $\sigma_{Cu}=7.1\times10^{7}\ \Omega^{-1}\,\mathrm{m}^{-1}$ and $\sigma_{Al}=8.0\times10^{7}\ \Omega^{-1}\,\mathrm{m}^{-1}$.

Two different measurement geometries are used to measure the spin valve effect in our device structure. In the conventional measurement geometry [Fig. 3(b)] the current is sent from contact 1 to 7 and the signal $R=V/I$ is measured between contacts 4 and 9, see Fig. 3(a). The conventional geometry suffers from a relatively large background resistance as compared to the spin valve resistance. Small parts of the ferromagnetic electrodes underneath the vertical Cu or Al wires of the cross are included in this background resistance, which can give rise to anisotropic magnetoresistance[50] (AMR) contributions and Hall effects. In the nonlocal measurement geometry [Fig. 3(c)] the current is sent from contact 1 to 5 and the signal $R=V/I$ is measured between contacts 6 and 9; see Fig. 3(a). This technique is similar to the ''potentiometric'' method of Johnson used in Refs. 34,35. However, the separation of the current and voltage circuits allows us to remove the AMR contribution and Hall effecs of the ferromagnetic electrodes completely: the (magneto)resistance of the current injecting contact (F1) is not relevant because any voltage drop that develops across it will not influence the current that is sent through it and similarly, no current flows through the ferromagnetic voltage contact (F2), so its (magneto)resistance does not affect the voltage measurement.

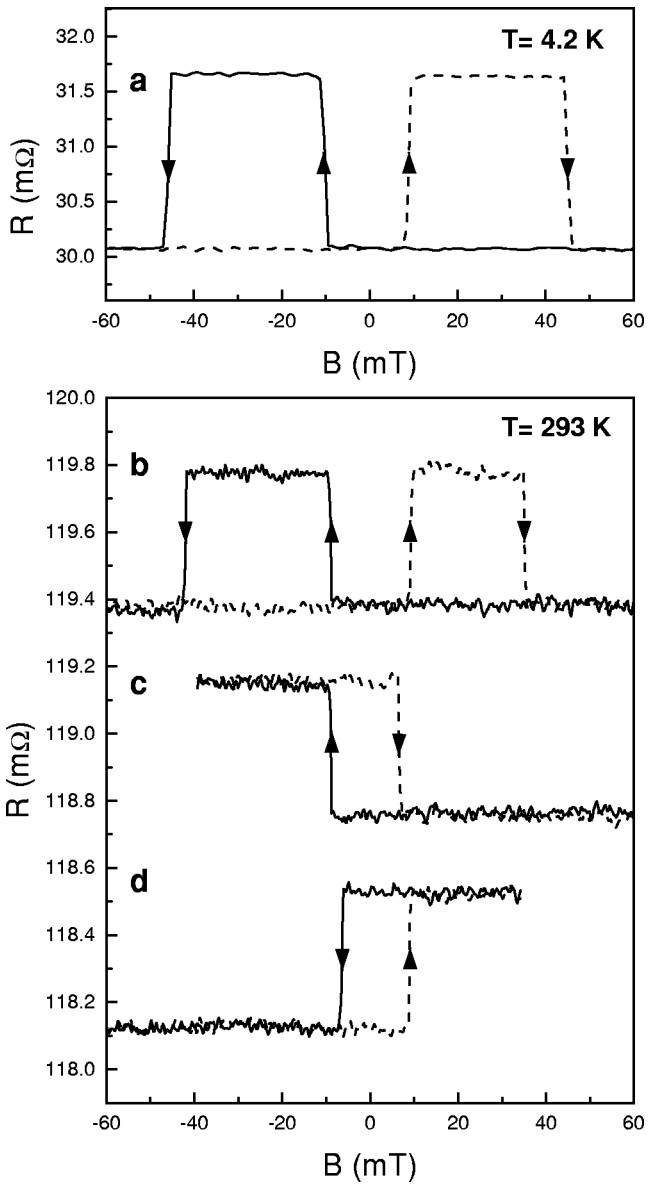

FIG. 4. The spin valve effect at $T=4.2$ K (a) and RT (b) in the nonlocal geometry for a Py/Cu/Py spin valve device (sample MSV1) with 250-nm Py electrode spacing. The solid (dashed) lines correspond to the negative (positive) sweep direction. (c),(d) illustrate the ''memory effect.'' For clarity the (c) and (d) are offset downwards. Note that the vertical scale of (a) is different from (b), (c), and (d).

VI. SPIN ACCUMULATION IN Py/Cu/Py SPIN VALVES

The measurements were performed by standard ac lock-in techniques, using current magnitudes of from 100 μA to 1 mA. Typical spin valve signals of two samples MSV1 and MSV2 (of the same batch) with a Py electrode spacing of $L=250$ nm are shown in the Figs. 4, 5, and 6. They are both measured in a nonlocal measurement geometry and conventional measurement geometry. Sample MSV1, data shown in Figs. 4 and 5, had a current injector Py1 electrode of size $2\times0.5\ \mu\mathrm{m}^2$, whereas detector electrode Py2 had a size of $14\times0.15\ \mu\mathrm{m}^2$. Sample MSV2, data in shown Fig. 6, had wider Py electrodes of $2\times0.8\ \mu\mathrm{m}^2$ and $14\times0.5\ \mu\mathrm{m}^2$. The first set of (narrower) Py electrodes [Py1,Py2] had a more ideal switching behavior and had 3 times larger switching fields as compared to the second set [Py1,Py2]. We note that a discussion of the magnetic behavior of the Py electrodes and contacts has been given in Ref. 20.

A. Nonlocal spin valve geometry

Figures 4(a) and 4(b) show typical data in the nonlocal measurement geometry taken at 4.2 K and RT for sample

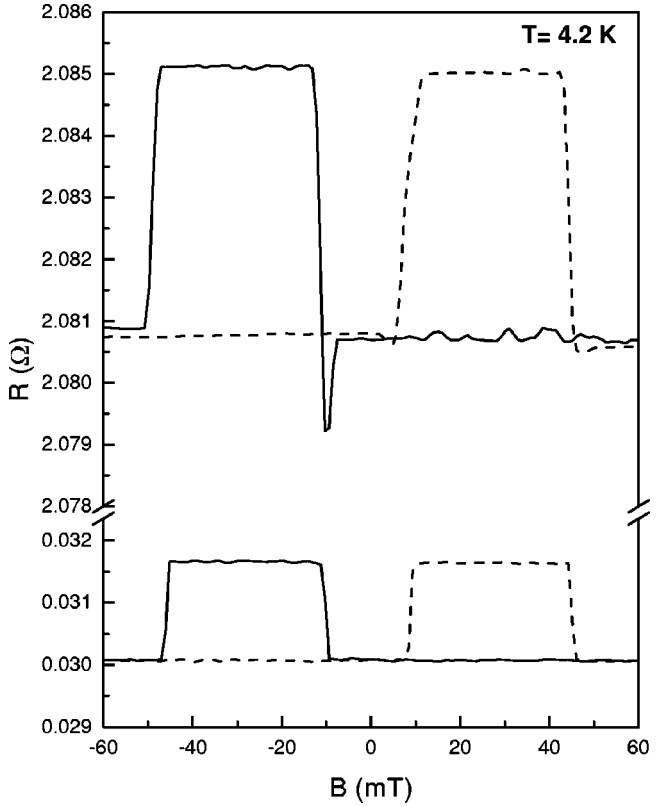

FIG. 5. The spin valve effect of sample MSV1 in a conventional measurement geometry (top curve) at $T=4.2$ K and nonlocal measurement geometry (bottom curve), with a Py electrode spacing $L=250$ nm. The sizes of the Py electrodes are 2×0.5 μm^2 (Py1) and 14×0.15 μm^2 (Py2). The solid (dotted) curve corresponds to a negative (positive) sweep direction of the **B** field.

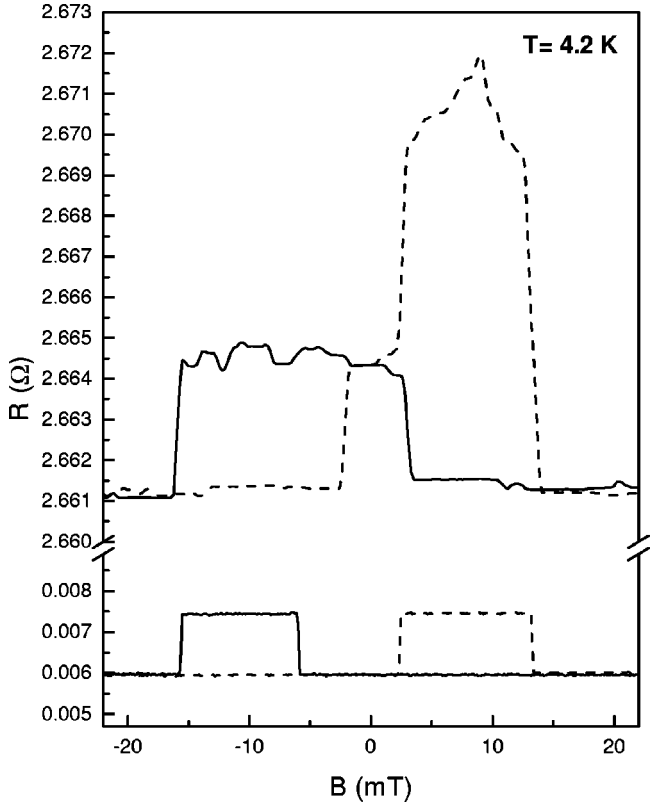

FIG. 6. The spin valve effect of sample MSV2 in a conventional measurement geometry (top curve) at $T=4.2$ K and nonlocal measurement geometry (bottom curve), with a Py electrode spacing $L=250$ nm. The sizes of the Py electrodes are 2×0.8 μm^2 (Py1) and 14×0.5 μm^2 (Py2). The solid (dotted) curve corresponds with a negative (positive) sweep direction of the **B** field.

MSV1 with a 250-nm Py electrode spacing. Sweeping the magnetic field from negative to positive field, an increase in the resistance is observed, when the magnetization of Py1 flips at 9 mT, resulting in an antiparallel magnetization configuration. The rise in resistance is due to the spin accumulation or equivalently an excess spin density present in the Cu metal. When the magnetization of Py2 flips at 47 mT ($T=4.2$ K) and 38 mT (RT), the magnetizations are parallel again, but now point in the opposite direction. The magnitude of the measured background resistance, around 30 mΩ at $T=4.2$ K and 120 mΩ at RT, depends on the geometrical shape of the Cu cross and is typically a fraction of the Cu square resistance.

Figures 4(c) and 4(d) show the ''memory effect.'' Coming from a high positive **B** field, the sweep direction of the *B* field is reversed after Py1 has switched, but Py2 has not. At the moment of reversing the sweep direction, the magnetic configuration of Py1 and Py2 is antiparallel, and accordingly a higher resistance is measured. When the **B** field is swept back to its original high positive value, the resistance remains at its increased level until Py1 switches back at a positive field of 9 mT. At zero **B** field the resistance can therefore have two distinct values, depending on the history of the Py electrodes.

B. Conventional spin valve geometry

The top curve in Fig. 5 shows the magnetoresistance behavior of sample MSV1 in the conventional measurement geometry. A small AMR contribution (dip in curve) of the Py1 electrode around -9 mT and a small Hall signal caused by the Py2 electrode can be observed in the negative sweep direction. Because a small part of the Py electrodes underneath the Cu wire is measured in this geometry, (local) changes in the magnetization at the Py/Cu contact area can produce an AMR or Hall signal.[20] In the positive sweep direction a dip is no longer observed, indicating that the magnetization reversal of the Py1 electrode is not the same for the two sweep directions. However, in the magnetic field range in between the two switching fields, we do observe a resistance ''plateau'' from 10 mT up to a field of 45 mT.

The magnitude of the spin valve effect measured in the conventional geometry is about 4.1 mΩ at $T=4.2$ K. This is about 2.5 times bigger than the magnitude of the spin signal measured in a ''nonlocal'' geometry (1.6 mΩ). Note that the factor of 2.5 is deviating from the factor of 2 as predicted by Eq. (17). This is attributed to deviations from our one-dimensional model, which can be expected for samples with the shortest Py electrode spacing $L=250$ nm, as the presence of the Cu side arms for these samples (see Fig. 3) are most felt.

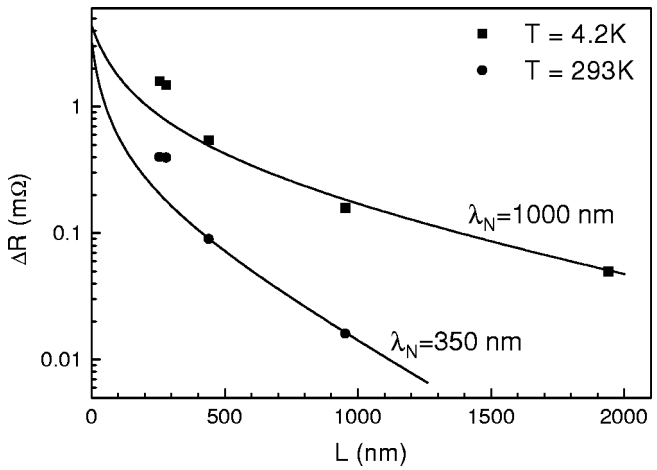

FIG. 7. Dependence of the magnitude of the spin signal ΔR on the Py electrode distance L, measured on Py/Cu/Py samples in the nonlocal geometry. The solid squares represent data taken at $T=4.2$ K; the solid circles represent data taken at RT. The solid lines represent the best fits based on Eq. (12).

The top curve in Fig. 6 shows the magnetoresistance behavior in the conventional measurement geometry for sample MSV2. Here a change of the resistance is already observed before the field has reached zero in a positive field sweep, whereas the negative field sweep is very asymmetrical compared to the positive field sweep. This is attributed to the formation of a multidomain structure in the 2×0.8 μm^2 (Py1) electrode, causing a large AMR (≈10 mΩ) signal at the Py/Cu contact area of the Py1 electrode.

However, in a nonlocal measurement geometry, the ''contact'' magnetoresistance contribution of the Py electrodes can be removed and a clear spin valve signal is observed with a similar magnitude as sample MSV1. This is shown in the bottom curve of Fig. 6. Note that the larger widths and aspect ratio of the Py electrodes in sample MSV2 result in 3 times smaller switching fields as compared to sample MSV1.

C. Dependence on Py electrode spacing

A reduction of the magnitude of spin signal ΔR is observed with increased electrode spacing L, as shown in Fig. 7. By fitting the data to Eq. (12) we have obtained the spin relaxation length λ_N in the Cu wire. From the best fits we find a value of 1 ± 0.2 μm at $T=4.2$ K and 350 ± 50 nm at RT. These values are compatible with those reported in literature, where 450 nm is obtained for Cu in CPP-GMR measurements at 4.2 K.[51] However, a detailed discussion of the obtained spin relaxation lengths and corresponding spin relaxation times will be given in Sec. IX.

In principle the fits of Fig. 7 also yield the spin polarization α_F and the spin relaxation length λ_F of the Py electrodes. However, the values of α_F and λ_F cannot be determined separately, as in the relevant limit ($M\gg1$) which applies to the Py/Cu/Py experiments ($12<M<26$), the spin signal ΔR is proportional to the product $\alpha_F\lambda_F$ as is shown by Eq. (14). From the fits we find that $\alpha_F\lambda_F=1.2$ nm at 4.2 K and $\alpha_F\lambda_F=0.5$ nm at RT. Taking, from literature,[40–42] a spin relaxation length in the Py electrode of $\lambda_F=5$ nm (at 4.2 K), a bulk current polarization of $\approx20\%$ in the Py electrodes at $T=4.2$ K is obtained: $\alpha_F=0.2$. We note, however, that the injected spin-polarized current from the Py electrode is partially shunted by the Cu wire lying on top of the Py electrode. When taken into account we estimate that it could increase the value $\alpha_F\lambda_F$ by a factor of 2–3.

It is also possible to calculate the polarization of the current at the Py/Cu interface. For a sample with a Py electrode spacing of $L=250$ nm at $T=4.2$ K and using Eq. (15) we find $P\simeq0.02$, a factor of 10 lower than the bulk polarization α_F of the Py electrodes. From the resistor model we can see why the current polarization at the Py/Cu interface is reduced. For this we need to calculate the magnitude of the spin-dependent resistance difference. Using Eq. (23) and $L=250$ nm, $\Delta R=1.6$ mΩ, $R^N_\square=0.3$ Ω, and $w=100$ nm (at $T=4.2$ K) we find $R_\downarrow-R_\uparrow\approx100$ mΩ. From the right-hand side term of Eq. (23) and using $R^F_\square=2$ Ω we can check that this indeed corresponds with the value of $\alpha_F\lambda_F\approx1.2$ nm, as was also obtained from the fit in Fig. 7. From Eqs. (18) and (19) and using $\lambda_F=5$ nm and $\alpha_F=0.2$ (at 4.2 K) we obtain the spin-up and spin-down resistance of the Py ferromagnet:

$$R^{Py}_\uparrow=\frac{2\lambda_F}{w(1+\alpha_F)}R^F{}_\square\approx160\ \text{m}\Omega, \tag{24}$$

$$R^{Py}_\downarrow=\frac{2\lambda_F}{w(1-\alpha_F)}R^F{}_\square\approx260\ \text{m}\Omega. \tag{25}$$

This shows that the total resistance experienced over a length $\lambda_F+\lambda_N$ by the spin-up and spin-down currents is indeed dominated by the spin-*independent* resistance $R^N+R=\lambda_N 2R^N_\square/w\simeq6$ Ω. Here we have used that $\lambda_N=1$ μm at $T=4.2$ K and $w=100$ nm. This leads to an interface polarization of $P\approx(R_\downarrow-R_\uparrow)/2(R^N+R)\approx1\%$ at the Py/Cu interface.

Although the role of interface resistance between two diffusive metals for spin injection will be described in the next section, we note here that the small difference $R_\downarrow-R_\uparrow\approx100$ mΩ responsible for a spin valve signal of $\Delta R=1.6$ $m\Omega$ could possibly also result from an interface resistance at the Py/Cu interface. Commonly reported resistivities of 5×10^{-16} Ω m^2 for the Py/Cu interface[40–42,46,52] and a contact area of $S=1\times10^{-14}$ m^2 (i.e., $R_{int}=50$ mΩ) would yield a realistic interface polarization of $\gamma=0.5$ for the Py/Cu interface, using Eq. (26). However, the specific details of the spin injection mechanism (interface, bulk, or a combination) do not alter the conclusion that the total spin-dependent resistance $R_\downarrow-R_\uparrow\approx100$ mΩ is dominated by the spin-independent resistance of the Cu strip over a spin relaxation length and hence leads to a considerable reduction of the spin valve signal, as was pointed out above.

D. Comparison with Johnson spin transistors

The magnitudes of the spin signals in the Py/Cu/Py samples, when scaled to the cross sections utilized in the Au thin film devices of Refs. 34 and 35 (the ''Johnson spin

transistor''), are more than 10^4 times smaller than those obtained in that previous work. In that earlier work it was necessary to invoke a spin polarization exceeding 100% to explain the results in terms of spin accumulation.[34,35] This contrasts with our results, which yield a spin polarization P of the current injected in the Cu wire at the Py/Cu interface of about 1%–2%.

In Refs. 34, 35, 53, and 54 Johnson postulates that spin injection is mediated by interfacial transport, because the interface resistances $R_{\uparrow}^{int}$ and $R_{\downarrow}^{int}$ would dominate the total resistance in both spin-up and spin-down channels: $R_{\uparrow}^{int} > R_{\uparrow}^{F}+R^{N}+R$ and $R_{\downarrow}^{int} > R_{\downarrow}^{F}+R^{N}+R$, respectively. Here $R_{\uparrow}^{F}$, $R_{\downarrow}^{F}$, R^{N}, and R are defined similarly as in Sec. IV. In this limit spin injection would be characterized by the interfacial spin injection parameter defined as

$$\gamma = \frac{R_{\downarrow}^{int} - R_{\uparrow}^{int}}{R_{\uparrow}^{int} + R_{\downarrow}^{int}}, \tag{26}$$

and Johnson derives the following expression for the spin accumulation signal:[16,35,53]

$$\Delta R = \frac{2\gamma^2 \lambda_N^2}{\sigma_N S L}. \tag{27}$$

Applying Eq. (27) Johnson calculates an expected spin signal of $\Delta R = 1.9\ \Omega$ for our Py/Cu/Py device with the shortest Py electrode spacing $L = 250$ nm, using $S = 5 \times 10^{-15}\ \mathrm{m}^2$, $\sigma_{Cu} = 7.1 \times 10^{7}\ \Omega^{-1}\,\mathrm{m}^{-1}$, $\gamma = 0.4$, and $\lambda_N = 1.0\ \mu\mathrm{m}$.[53]

However, a polarization of the current at the Py/Cu interface of $\gamma = 40\%$ would require spin-dependent interface resistances of $R_{\uparrow}^{int} = 16\ \Omega$ and $R_{\downarrow}^{int} = 37\ \Omega$ to overcome the conductance mismatch. The obtained interface resistances are calculated using Eqs. (26) and (21) and replacing Eqs. (18) and (19) by

$$R_{\uparrow} = R_{\uparrow}^{int} + R_{\uparrow}^{F} + R^{N}, \tag{28}$$

$$R_{\downarrow} = R_{\downarrow}^{int} + R_{\downarrow}^{F} + R^{N}, \tag{29}$$

where the spin-dependent interface resistances $R_{\uparrow}^{int}$ and $R_{\downarrow}^{int}$ have simply been added up to bulk spin-dependent resistances $R_{\uparrow}^{F}$ and $R_{\downarrow}^{F}$ because the spin polarization γ and the bulk spin polarization α_F are found to be positive ($\alpha_F > 0$ and $\gamma > 0$) for Py and Cu.[55] The values $R_{\uparrow}^{int} = 16\ \Omega$ and $R_{\downarrow}^{int} = 37\ \Omega$ yield a total single interface resistance $R_{int} = 11\ \Omega$ or, equivalently, a interface resistivity of $1 \times 10^{-13}\ \Omega\,\mathrm{m}^2$. This is more than a 100 times larger then the upper limit $0.1\ \Omega$ or equivalently a contact resistivity of $1 \times 10^{-15}\ \Omega\,\mathrm{m}^2$ that we are able to determine from our Py/Cu/Py spin valve experiment in a conventional measurement geometry; see Figs. 5 and 6.

The above arguments also apply for the experiment of Refs. 34 and 35 where a gold layer is sandwiched in between two Py layers. There is no physical reason why there should exist an interface resistivity larger than $1 \times 10^{-13}\ \Omega\,\mathrm{m}^2$ between the Au and Py or Co layers in the experiment of Ref. 34, which can explain an interface current polarization of $\gamma = 0.4$ or more. Equation (27) can therefore not be applied to the experiment of Ref. 34, because it does not include the (fast) spin relaxation reservoirs of the ferromagnetic injector and detector contacts, which dominate the total spin relaxation in the case of transparent contacts, as was already pointed out in Refs. 36 and 37.

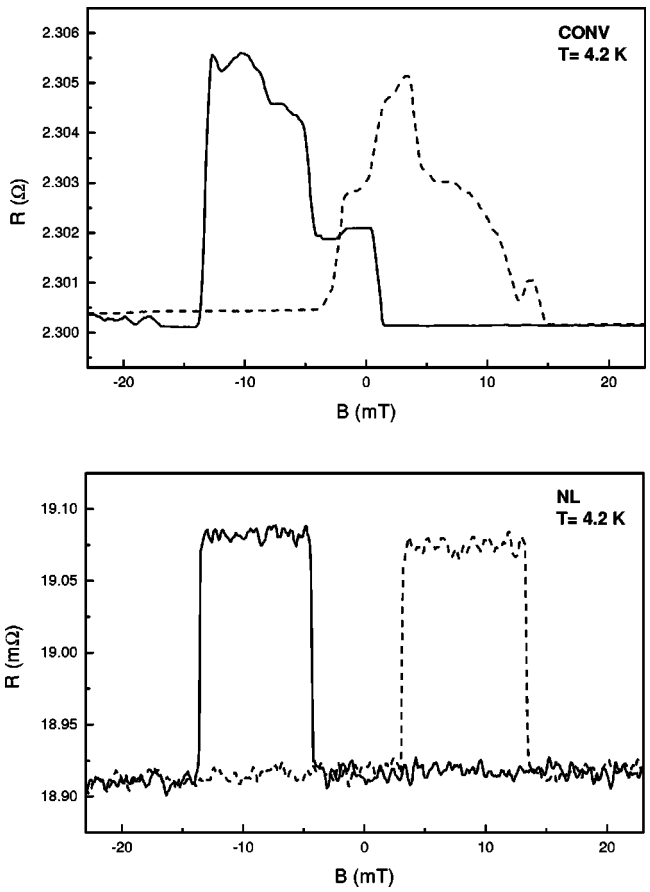

FIG. 8. The spin valve effect of a Py/Al/Py sample using a conventional measurement geometry (CONV, top curve) at $T = 4.2$ K and nonlocal measurement geometry (NL, bottom curve), with a Py electrode spacing $L = 250$ nm. The sizes of the Py electrodes are $2 \times 0.8\ \mu\mathrm{m}^2$ (Py1) and $14 \times 0.5\ \mu\mathrm{m}^2$ (Py2). The solid (dotted) curve corresponds with a negative (positive) sweep direction of the **B** field.

In view of this, given the unexplained discrepancies ($\gamma > 1$) of the earlier work in Refs. 34 and 35, and the more consistent values obtained in the recent work, it is our opinion that the results of Refs. 34 and 35 cannot be reconciled with spin injection and spin accumulation.

VII. SPIN ACCUMULATION IN Py/Al/Py SPIN VALVES

Here we will describe spin injection experiments using Permalloy $Ni_{80}Fe_{20}$ (Py) strips as ferromagnetic electrodes to drive a spin-polarized current via transparent contacts into aluminum (Al) crossed strips; see Fig. 3. Similar current polarizations and spin relaxation lengths for Py and Al are obtained as in the previous section (Sec. VI).

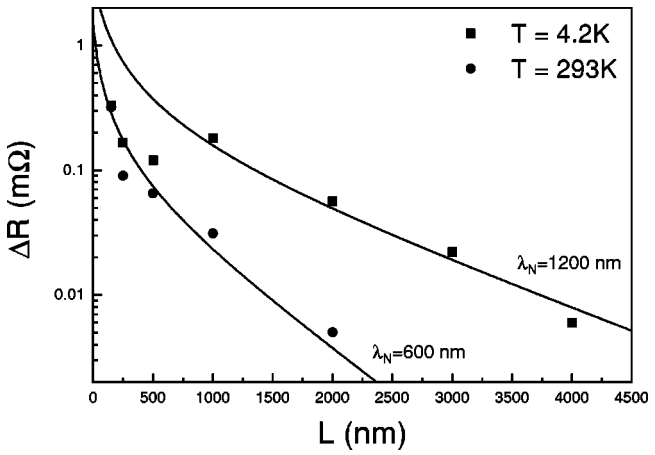

FIG. 9. Dependence of the magnitude of the spin signal ΔR on the Py electrode distance L, measured in the nonlocal geometry for Py/Al/Py spin valves. The solid squares represent data taken at $T=4.2$ K; the solid circles represent data taken at RT. The solid lines represent the best fits based on Eq. (12).

A. Spin valve measurements

Figure 8 shows a typical spin valve signal of a Py/Al/Py sample with a Py separation spacing of $L=250$ nm and Py electrodes of sizes 2×0.8 μm^2 and 14×0.5 μm^2.

The top curve in Fig. 8 shows the magnetoresistance behavior in the conventional measurement geometry. Again the magnetoresistance signals of the Py contacts are dominating in this geometry, reaching a maximal amplitude of about 6 mΩ. Note that the two resistance values at high positive and negative magnetic fields differ by a value of about 0.3 mΩ, which is attributed to a local Hall effect caused by the 14×0.5 μm^2 Py electrode. The bottom curves in Fig. 8 show magnetic field sweeps in the nonlocal measurement geometry, which clearly shows a spin valve signal having removed all the spurious contact magnetoresistance effects. The magnitude of the spin valve signal measured is 0.18 mΩ at 4.2 K.

B. Dependence on Py electrode spacing

A reduction of the magnitude of spin signal ΔR of the Py/Al/Py samples is observed with increased electrode spacing L, as shown in Fig. 9. However, for the $T=4.2$ K data this dependence is not monotonic. The spin valve devices with small $L=250$ nm and $L=500$ nm show a smaller spin valve signal than the device with $L=1$ μm. We note that all the devices shown in Fig. 9 are from the same (processing) batch. However, the granular structure of the Al film with a grain size on the order of the width of the Al strip causes fluctuations in the resistance of the Al strip in between the Py electrodes. The samples with $L=250$ nm and $L=500$ nm indeed show a higher resistance than expected when measured in the conventional geometry at $T=4.2$ K. This irregular behavior of the resistance due to grains is not observed at RT due to the additional presence of electron-phonon scattering. From the best fits to Eq. (12) we find a spin relaxation length λ_N in Al of 1.2 ± 0.2 μm at $T=4.2$ K and 600 ± 50 nm at RT. Note that the spin relaxation lengths are about 2 times larger than reported in Ref. 21. The reason for this increase is the higher conductivity of the Al in these samples, caused by a lower background pressure of 1×10^{-8} mbar during evaporation as compared to a background pressure of 1×10^{-6} used in Ref. 21.

The fits of Fig. 9 also yield the spin polarization α_F and the spin relaxation length λ_F of the Py electrodes. We find $\alpha_F\lambda_F=1.2$ nm at 4.2 K and $\alpha_F\lambda_F=0.5$ nm at RT, in agreement with the Py/Cu/Py spin valve data of Sec. VI. Note that for the Py/Al/Py spin valve also applies that $M\gg1$ and thus the spin signal ΔR is proportional to the product $\alpha_F\lambda_F$ ($25<M<32$). Using Eq. (15), a polarization P for the Py/Al/Py sample with the smallest Py electrode spacing of $L=250$ nm at $T=4.2$ K is found to be only 3%: $P=0.03$.

VIII. SPIN INJECTION USING Co AND Ni FERROMAGNETIC ELECTRODES

From Eq. (23) it can be seen that the magnitude of the spin-dependent resistance $R_\downarrow-R_\uparrow$ is sensitive to the properties α_F, λ_F, and σ_F of the ferromagnet. As $R_\downarrow-R_\uparrow$ enters squared in the spin valve signal ΔR [see Eq. (21)], an increase of λ_F with a factor of 10 would increase ΔR with a factor of 100. We have therefore tried cobalt (Co) and nickel (Ni) as ferromagnetic spin injectors and detectors to increase the magnitude of the spin valve signal, as larger spin relaxation lengths can be expected for these materials.[5,6]

A. Spin accumulation in Co/Cu/Co spin valves

Figure 10(a) shows a ''contact'' magnetoresistance trace and magnetic switching behavior at RT of a 14×0.5 μm^2 (Co2) electrode of a Co/Cu/Co spin valve device with a Co electrode spacing of 250 nm and Co electrodes of sizes 2×0.8 μm^2 and 14×0.5 μm^2. The ''contact'' magnetoresistance is measured by sending current from contact 5 to 7 and measuring the voltage between contacts 6 and 9 [see Fig. 3(a)]. Note that in this geometry the measured voltage is not sensitive to a spin valve signal as only one Co electrode is used in the measurement configuration. The magnetoresistance traces of Fig. 10(a) indicate a clear switching of the magnetization at 20 mT of the 14×0.5 μm^2 Co2 electrode and is attributed to a local Hall effect produced at the Co/Cu contact area of the Co2 electrode.

Figure 10(b) shows the spin valve effect in the nonlocal measurement geometry at RT for a Co/Cu/Co spin valve device. The magnitude of the spin-dependent resistance $\Delta R=0.25$ mΩ is slightly smaller than in the Py/Cu/Py spin valve device. At $T=4.2$ K the signal increases to $\Delta R=0.8$ mΩ. Using Eq. (12) and the values of σ_N, λ_N for Cu and σ_F for Co (see Sec. V), we obtain $\alpha_F\lambda_F=0.3$ at RT and $\alpha_F\lambda_F=0.7$ at $T=4.2$ K. These obtained values are much smaller than reported for Co in CPP-GMR experiments, where $\alpha_F\approx0.5$ and $\lambda_F=10$–60 nm.[40,56–59] This discrepancy will be discussed in Sec. IX C.

B. Spin accumulation in Ni/Cu/Ni spin valves

In Figs. 11(a) and 11(b) two ''contact'' magnetoresistance traces of a Ni electrode (Ni1) with size 2×0.5 μm^2 (top

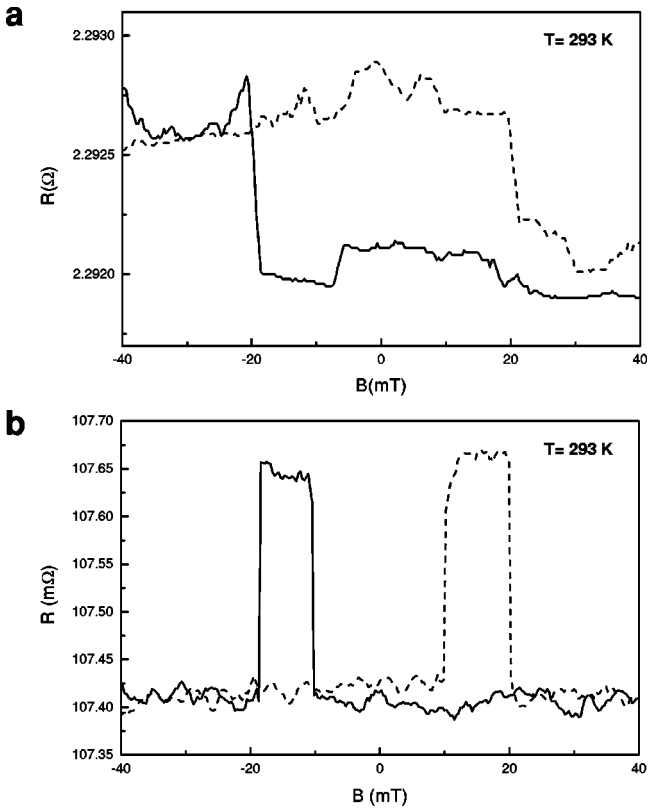

FIG. 10. (a) ''Contact'' magnetoresistance trace of the Co2 electrode with size $14\times0.5\ \mu m^2$. The Hall signal indicates an abrupt magnetization switching of the Co2 electrode. (b) The spin valve effect at RT in a Co/Cu/Co device with a Co electrode spacing $L=250$ nm, using the nonlocal measurement geometry. The solid (dotted) curve corresponds with a negative (positive) sweep direction of the **B** field.

curve) and a Ni electrode (Ni2) with size $14\times0.15\ \mu m^2$ (middle curve) are shown of a Ni/Cu/Ni spin valve device with a Ni electrode spacing of 500 nm. For the Ni1 contact current is send from contact 1 to 5 and the voltage is measured from contact 4 to 6 (see Fig. 3). For the Ni2 contact current is send from contact 5 to 7 and the voltage is measured from contact 6 to 9. In the magnetic field sweeps of Figs. 11(a) and 11(b) a large range can be observed where the magnetization configurations of the Ni electrodes are antiparallel. We note that the magnetic field in the measurements of Fig. 11 is applied perpendicular to the long axis of the Ni electrodes, showing a more pronounced magnetic switching behavior than an applied magnetic field along the long axis of the Ni electrodes. However, no spin valve signal could be detected within experimental accuracy in the nonlocal measurement geometry at RT as well as at $T=4.2$ K, as is shown in Fig. 11(c) (RT). An upper bound on the spin valve signal is found to be $\Delta R<20\ \mu\Omega$ at RT as well as at $T=4.2$ K. Using Eq. (12) and the values of σ_N and λ_N for Cu and σ_F for Ni (see Sec. V), we obtain $\alpha_F\lambda_F<0.3$ at RT as well as at $T=4.2$ K. These obtained values are smaller than reported for Ni in GMR experiments, where $\alpha_F\approx0.2$ (Refs. 55 and 60) and using an expected $\lambda_F(\mathrm{calc})=15$ nm

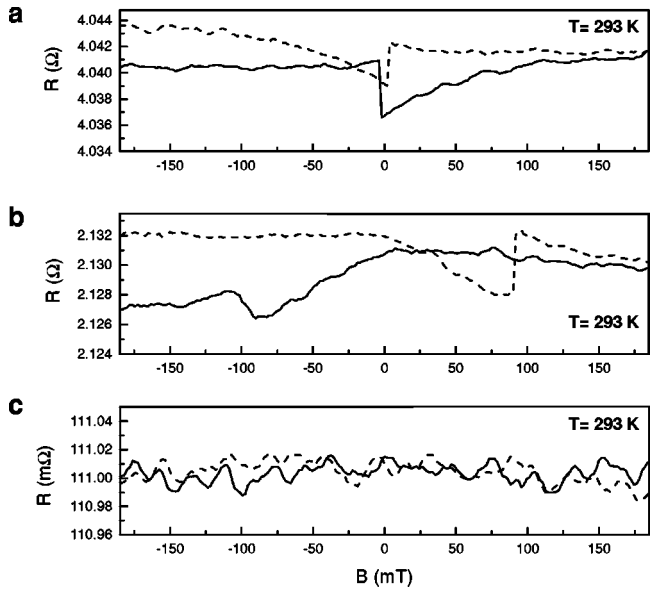

FIG. 11. (a) ''Contact'' magnetoresistance trace (see text) of the Ni1 electrode with size $2\times0.5\ \mu m^2$. (b) ''Contact'' magnetoresistance trace of the Ni2 electrode with size $14\times0.15\ \mu m^2$. (c) The spin valve effect of a Ni/Cu/Ni device at RT with a Ni electrode spacing of $L=500$ nm, using a nonlocal measurement geometry. The solid (dotted) curve corresponds with a negative (positive) sweep direction of the **B** field.

for Ni. The spin relaxation length $\lambda_F(\mathrm{calc})$ and the observed discrepancy will be calculated and discussed in Sec. IX C.

IX. SPIN RELAXATION TIMES OF CONDUCTION ELECTRONS IN METALS

In this section we will analyze our obtained spin relaxation length λ_{sf} in Cu and Al from the spin injection experiments in Secs. VI, VII, and VIII and compare the associated spin relaxation times τ_{sf} with theory and previously reported values from CPP-GMR,[61] CESR,[62] weak localization,[63] and superconducting tunneling experiments.[7] The obtained spin polarization and spin relaxation lengths in Py, Co, and Ni will be compared with reported values from CPP-GMR experiments.

In CESR experiments the transverse relaxation time T_2 is measured, which is proportional to the width of the absorption peak at the resonance frequency. Yafet[64] showed that in metals T_2 is equal to the longitudinal spin relaxation time T_1 ($T_1=\tau_{sf}$). In weak localization and superconducting tunneling experiments the spin-orbit scattering time $\tau_{s.o.}$ is determined, with $\tau_{s.o.}$ being defined similarly in both experiments.[65] The spin-orbit interaction in weak localization experiments is responsible for the destructive interference when electrons are scattered at (nonmagnetic) impurities,[63] whereas in the superconducting tunneling experiments it mixes up the spin-up and spin-down quasiparticle density of states, when they are Zeeman split by an applied magnetic field.[7,66] We make the identification $\tau_{s.o.}=\tau_{sf}$.

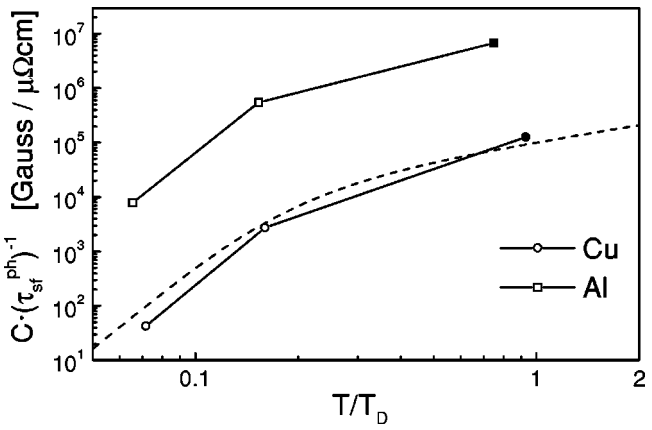

FIG. 12. The (revised) Bloch-Grüneisen plot (Ref. 69). The quantity $C(\tau_{sf}^{ph})^{-1}$ is plotted vs the reduced temperature T/T_D on logarithmic scales, where $C=(\gamma_L(\lambda/\Delta E)^2\rho_D)^{-1}$. Here $(\tau_{sf}^{ph})^{-1}$ is the electron-phonon-induced spin relaxation rate and $\gamma_L=1.76\times10^7$ Gauss^{-1} sec^{-1}. We used $\rho_D=1.5\times10^{-8}$ Ω m and $T_D=315$ K for Cu and $\rho_D=3.3\times10^{-8}$ Ω m and $T_D=390$ K for Al (Refs. 62 and 70). The dashed line represents the general Bloch-Grüneisen curve. The open squares represent Al data taken from CESR and the JS spin injection experiment (Refs. 17 and 72). The open circles represent Cu data taken from CESR experiments (Refs. 73–75). The solid square (Al) and circle (Cu) are values from the spin injection experiments described here and Refs. 19 and 21.

A. Electron spin relaxation in nonmagnetic metals

The fact that a spin can be flipped implies that there is some mechanism which allows the electron spin to interact with its environment. In the absence of magnetic impurities in the nonmagnetic metal, the dominant mechanism providing for this interaction is the spin-orbit interaction, as was argued by Elliot[64] and Yafet.[67] When included in the band structure calculation of a nonmagnetic metal the result of the spin-orbit interaction is that the Bloch eigenfunctions become linear combinations of spin-up and spin-down states, mixing some spin-down character into the predominantly spin-up states and vice versa.[68] Using a perturbative approach Elliot showed that a relation can be obtained between the elastic scattering time (τ_e), the spin relaxation time (τ_{sf}), and the spin-orbit interaction strength defined in Ref. 69 as $(\lambda/\Delta E)^2$:

$$\frac{\tau_e}{\tau_{sf}}=a\propto\left(\frac{\lambda}{\Delta E}\right)^2, \tag{30}$$

where λ is the atomic spin-orbit coupling constant for a specific energy band and ΔE is the energy separation from the considered (conduction) band to the nearest band which is coupled via the atomic spin orbit interaction constant. Yafet has shown that Eq. (30) is temperature independent.[64] Therefore the temperature dependence of $(\tau_{sf})^{-1}$ scales with the temperature behavior of the resistivity being proportional to $(\tau_e)^{-1}$. For many clean metals the temperature behavior of the resistivity is dominated by the electron-phonon scattering and can to a good approximation be described by the Bloch-Grüneisen relation[70] $(\tau_{sf})^{-1}\sim T^5$ at temperatures below the Debye temperature T_D and $(\tau_{sf})^{-1}\sim T$ above T_D. Using data from CESR experiments, Monod and Beuneu[69,71] showed that $(\tau_{sf})^{-1}$ follows the Bloch-Grüneisen relation for (clean) monovalent alkali and noble metals. In Fig. 12 their results are replotted for Cu and Al, normalized to the resistivity ρ_D at $T=T_D$.[68] In addition we have plotted the obtained data points for Cu and Al at $T/T_D\approx1$ from our spin injection experiments by calculating τ_{sf}^{ph} from λ_{sf} (see Sec. IX B below) and using the calculated atomic spin orbit strength parameters from Ref. 71: $(\lambda/\Delta E)^2=2.16\times10^{-2}$ for Cu and $(\lambda/\Delta E)^2=3\times10^{-5}$ for Al.

From Fig. 12 it can be seen that for Cu the Bloch-Grüneisen relation is well obeyed, *including* the newly added point deduced from our spin injection experiments at RT $(T/T_D=0.9)$. For Al, however, the previously obtained data points as well as the newly added point from the injection experiments at RT $(T/T_D=0.75)$ are deviating from the general curve, being about two orders of magnitude larger than the calculated values based on Eq. (30). We note that we cannot extract data for the Bloch-Grüneisen plot shown in Fig. 12 from our spin injection experiments at $T=4.2$ K, because the impurity (surface) scattering rate is dominating the electron-phonon contribution at $T=4.2$ K.

Fabian and Das Sarma have resolved the discrepancy for Al by pointing out that there can exist so called ''spin hot spots'' at the Fermi surface of polyvalent metals (like Al). Performing an *ab initio* pseudopotential band structure calculation of Al they showed that the spin flip contributions of these (small) spin-hot-spot areas on the (large) Fermi surface dominate the total spin relaxation rate $(\tau_{sf})^{-1}$, making it factor of 100 faster than expected from the Elliot-Yafet relation [Eq. (30)].[76–78] Our newly added data point shows that the underestimation of the spin-orbit strength also holds for Al at RT $(T/T_D=0.75)$, as can be seen in Fig. 12. However, it is in excellent agreement with the theoretical predicted value by Fabian and Das Sarma[78] as will be shown below.

B. Quantative analysis of the spin relaxation time τ_{sf} in Cu and Al

Comparing the conductivities and spin relaxation lengths at RT and $T=4.2$ K we can obtain the impurity and electron-phonon scattering rate and their associated spin relaxation rates. Therefore we can define an impurity spin relaxation ratio $a^{imp}=\tau^{imp}/\tau_{sf}^{imp}$ and an electron-phonon spin relaxation ratio $a^{ph}=\tau^{ph}/\tau_{sf}^{ph}$. Here $(\tau^{imp})^{-1}$ and $(\tau^{ph})^{-1}$ are the impurity and electron-phonon scattering rate and $(\tau_{sf}^{imp})^{-1}$ and $(\tau_{sf}^{ph})^{-1}$ are the impurity- and electron-phonon-induced spin relaxation rate. From the measured conductivity at $T=4.2$ K and Eq. (2) we can determine $(\tau^{imp})^{-1}$. Using the Mathiessen rule $(\tau_e)^{-1}=(\tau^{imp})^{-1}+(\tau^{ph})^{-1}$ and the RT conductivity we can determine $(\tau^{ph})^{-1}$. We note that the surface scattering in our samples is dominating the impurity scattering, as the mean free paths of $l_e\approx60$ nm for both Al and Cu at $T=4.2$ K are larger than their film thicknesses (50 nm). In the calculation we use the free electron values $N(E_F)_{\mathrm{Cu}}=1.8\times10^{28}$ states/eV/m^3 and $v_F(\mathrm{Cu})=1.57$

TABLE I. Comparison of spin relaxation times between different experiments. τ_{sf}^{imp} [ps] is the impurity-induced spin relaxation time at low temperatures $T \leqslant 4.2$ K due to surface scattering, dislocations or grain boundaries. τ_{sf}^{ph} [ps] is the electron-phonon-induced spin relaxation time at elevated temperatures due to the electron-phonon scattering. λ_N^{ph} is the electron-phonon scattering induced spin relaxation length at RT; see text. For the definition of a^{imp} and a^{ph} see text.

	τ_{sf}^{imp} [ps]	a^{imp}	τ_{sf}^{ph} [ps]	a^{ph}	λ_N^{ph} [nm][a]	Ref.
Aluminum (Al)						
Theory	-	-	90[a]	1.2×10^{-4} [a]	-	78
Spin injection	100	0.6×10^{-4}	85[a]	1.1×10^{-4} [a]	780[a]	21
Spin injection	70	3.7×10^{-4}	124[a]	1.3×10^{-4} [a]	1200[a]	This work
Spin injection (JS)	9000	15×10^{-4}	4000[b]	4.8×10^{-4} [b]	-	17
CESR	3000–9000	9.0×10^{-4}	1000–57 000[c]	2.6×10^{-4} [c]	-	72,74,78
Antiweak localization	4–46	$(0.2–1.2)\times10^{-4}$	-	-	-	81,82
Superconducting tunneling	8–160	$(0.1–5)\times10^{-4}$	-	-	-	7,83–85
Copper (Cu)						
Spin injection	41	0.7×10^{-3}	14[a]	2.0×10^{-3} [a]	560[a]	This work, 19
CESR	2000–9000	0.8×10^{-3}	2000–21 000[d]	1.1×10^{-3} [d]	-	73,74
GMR	4	19×10^{-3}	-	-	-	51
Antiweak localization	5	1.3×10^{-3}	-	-	-	81,82
Energy-level spectroscopy	20–80	-	-	-	-	86

[a]For $T=293$ K
[b]For $T=45$ K
[c]For a temperature range $T=[1–90]$ K.
[d]For a temperature range $T=[1–60]$ K.

$\times10^6$ m/s for Cu (Ref. 79) and we use $N(E_F)_{Al}=2.4\times10^{28}$ states/eV/m^3 and $v_F(\mathrm{Al})=1.55\times10^6$ m/s for Al (Ref. 80).

The obtained parameters for Cu and Al (τ_{sf}^{imp}, τ_{sf}^{ph}, a^{imp}, a^{ph}) are tabulated in Table I. From Table I we see that τ_{sf}^{ph} and a^{ph} for Al at RT from our spin valve experiments are in good agreement with the theoretical values as predicted in the band structure calculation by Fabian and Das Sarma.[78] They are also in agreement with the results obtained from CESR experiments and the earlier JS spin injection experiments at temperatures below 90 K. Note that in those earlier experiments the spin relaxation times are two to three orders of magnitude larger due the use of extremely clean samples with electron mean free paths of a few tens of micrometers. Also for Cu we see that τ_{sf}^{ph} and a^{ph} at RT are in good agreement with the results obtained from CESR experiments at temperatures below 60 K.

The impurity scattering ratio a^{imp} shows a much bigger spread in values for both Al and Cu. We speculate that this due to the different origins of the impurities in the samples used for the various measurement techniques. For the CESR experiments the impurity scattering is caused by dislocations, whereas for our experiment and the weak localization and superconducting tunneling experiments, it is mainly due to surface and grain boundary scattering.

We note that for the thin films we use it is not possible to realize mean free paths of the order of micrometers as they will always be limited by surface scattering. However, the sensitivity of the CESR technique does not allow measurements of τ_{sf}^{ph} below typically 1 ns, whereas the superconducting quantum interference device (SQUID) detection technique used in Ref. 17 does not operate at RT. Therefore spin injection into thin films is rather complementary to the CESR techniques and the JS spin injection experiments in determining τ_{sf}^{ph} in the temperature range from liquid helium to RT; see Fig. 12.

The fact that about half of the momentum scattering processes in the Al and Cu thin films at RT is due to electron-phonon scattering limits the maximum obtainable spin relaxation length in Al and Cu at RT. This is illustrated by calculating the electron-phonon-scattering-induced spin relaxation length at RT: $\lambda_N^{ph}=v_F\tau^{ph}(\sqrt{1/3a^{ph}})$. This is the maximal obtainable spin relaxation length at RT, being limited by electron-phonon scattering. The calculated values of λ_N^{ph} are shown in Table I and indicate that the experimentally obtained spin relaxation lengths at RT in Al and Cu thin films, as presented in this paper, can be maximally improved by a factor of about 2.

C. Spin injection efficiency of Py, Co, and Ni ferromagnets

In addition to the spin-orbit interaction, as described above for nonmagnetic metals, in metallic ferromagnets spin flip scattering can be caused by magnons.[43] The spin flip scattering by magnons has two effects. It will add to the spin flip scattering rate originating from the spin-orbit interaction, which reduces the spin relaxation length λ_F of the ferromagnet at higher temperatures. Second, it will lower the bulk current polarization of the ferromagnet α_F by (1) changing $\sigma_\uparrow$ and $\sigma_\downarrow$ and in addition by (2) giving rise to a ''spin mixing rate'' which equalizes the spin-up and spin-down currents in the ferromagnet.[43] The presence of spin flip scattering by magnons can therefore lower α_F as well as λ_F at RT.

TABLE II. Spin injection efficiencies $\alpha_F\lambda_F$ in nm for three different ferromagnetic metals. The data is deduced from the mesoscopic spin valve (MSV) experiments with transparent contacts in a nonlocal geometry using Cu as nonmagnetic metal and compared with results from CPP-GMR experiments.

	$Ni_{80}Fe_{20}$		Co		Ni	
	4.2 K	RT	4.2 K	RT	4.2 K	RT
$\alpha_F\lambda_F$ MSV	1.2	0.5	0.7	0.3	< 0.3	<0.3
$\alpha_F\lambda_F$ GMR	3.6–4.0[a]	-	4.5–27.7[b]	8.1–15.5[b]	3[c]	-

[a]From Refs. 40–42.
[b]From Refs. 5, 6, and 56–59.
[c]From Refs. 55 and 60 ($\alpha_{Ni}=0.2$) and using $\lambda_{Ni}(\text{calc})=15$ nm.

At low temperatures ($T<100$ K) and in the absence of magnetic impurities an upper estimate can be given for the expected spin relaxation length in Co and Ni due to the spin-orbit interaction:[57] $\lambda_F=v_F\tau_e(\sqrt{1/3a})$, where a is taken from spin flip scattering cross sections determined by CESR experiments:[55,87] $a_{Fe}=1.1\times10^{-2}$, $a_{Ni}=1.5\times10^{-2}$, and $a_{Co}=4.2\times10^{-2}$. Using a free electron model, the spin relaxation lengths λ_{Py} for Py with $\sigma_{Py}=8.1\times10^6\ \Omega^{-1}\text{m}^{-1}$ and λ_{Co} for Co with $\sigma_{Co}=1.7\times10^7\ \Omega^{-1}\,\text{m}^{-1}$ have been estimated in this way in Ref. 40: $\lambda_{Py}(\text{calc})\approx9$ nm and $\lambda_{Co}(\text{calc})\approx36$ nm at $T=4.2$ K. Note that λ_F scales linearly with τ_e and thus the conductivity of the ferromagnetic metal. For Ni we derive an estimate of λ_F using a free electron density of $5.4\times10^{28}\ \text{m}^{-3}$. With $\sigma_{Ni}=1.6\times10^7\ \Omega^{-1}\,\text{m}^{-1}$ and $a_{Ni}=1.5\times10^{-2}$ we then calculate $\lambda_{Ni}(\text{calc})=15$ nm at $T=4.2$ K.

Because $M>10$ for all our spin valve samples, we cannot separately determine α_F and λ_F from the magnitude of the spin valve signal ΔR. In Table II we therefore give the ''spin injection efficiency'' $\alpha_F\lambda_F$ together with reported values from CPP-GMR experiments. We note that our thin film conductivities for Py, Co, and Ni are within a factor of 2 of the reported conductivities in the CPP-GMR experiments.

Table II shows that our obtained spin injection efficiency of the Py ferromagnet $\alpha_{Py}\lambda_{Py}$ is in quantative agreement with the values reported in CPP-GMR experiments ($\alpha_{Py}=0.7$, $\lambda_{Py}=5$ nm), taking into account that our obtained $\alpha_{Py}\lambda_{Py}$ represents a minimal value due to a partially shunting of the injected current by the Cu wire on top of the Py electrodes. The reduction of $\alpha_{Py}\lambda_{Py}$ at RT beyond the ratio 1.8 of the Py conductivies at $T=4.2$ K and RT could be attributed to magnons lowering α_F at RT.

For the Co and Ni ferromagnets we observe spin injection efficiencies $\alpha_F\lambda_F$ which are more than one order of magnitude smaller than values of $\alpha_F\lambda_F$ obtained in CPP-GMR experiments. So the question is, what is causing this rather large reduction of the spin injection efficiency?

First we discuss the possible influences of an existing interface resistance at the Co/Cu and Ni/Cu interfaces. From the resistance measured in a conventional geometry we are able to determine an upper estimate of the (diffusive) interface resistances. For the Co/Cu/Co spin valve of Fig. 10 we find an upper limit for a single Co/Cu interface of 0.4 Ω, whereas for the Ni/Cu/Ni spin valve of Fig. 11 we find for a single Ni/Cu interface 0.6 Ω. We note that the associated Co/Cu interface resistivity ($\approx4\times10^{-15}\ \Omega\,\text{m}^2$) values is about 4 times larger than calculated for Co/Cu (specular or diffusive) interfaces[4,88–90] and also 5 times larger than values obtained from CPP-GMR experiments.[52,56] In case these Co/Cu and Ni/Cu interface resistances are spin dependent, the spin signal would be (largely) increased as the sign of the bulk and interface spin asymmetries of Co, Ni, and Cu are found both to be positive.[55,89–91] However, this is clearly not observed. In the opposite case of spin-independent interface resistances, the interface resistance for each spin channel ($\approx1\ \Omega$) will not reduce the measured spin valve signal much as the spin-independent interface resistance just adds to the (larger) spin-independent resistance of the Cu strip of about 6 Ω [see Sec. VI D, Eqs. (28) and (29)]. Therefore, the presence of the interface resistance could only reduce the spin signal by additional spin flip scattering, an effect which has recently been studied in CPP-GMR spin valves.[92,93] The physical origin of this mechanism could be diverse, for instance: surface roughness creating local magnetic fields due to the formation of random domains or the formation of antiferromagnetic oxides CoO and NiO at the surface during the time in between the Kaufmann sputtering and the Cu or Al deposition. However, as we do not have a characterization of the interfacial structure we cannot analyze what could be the most probable cause.

Second, a deviation in the bulk properties of the Co and Ni could explain the small spin injection efficiencies. Although in our opinion it is not likely that the bulk spin relaxation length would be subdue to a substantial shortening, a reduction of the polarization α_F in our Co and Ni ferromagnets might occur. In CIP-GMR experiments[94] a strong decrease of more than an order of magnitude in the GMR signal was reported upon changing the base (H_2O) pressure in the vacuum chamber from 10^{-8} to 10^{-5} mbar, just before deposition of the Co and Cu layers. In our deposition chamber the base pressure is only 10^{-7} mbar, whereas in the experiments, e.g., on Co/Ag multilayers[56] the base pressure is of the system is 10^{-8} mbar. Theoretical work[91] predicts $\alpha_{Co}\approx0.6$ for fcc Co with a conductivity close to our Co thin film. However, we do not know the crystallinity and/or the crystal orientation of our Co films, which complicates a direct comparison to Ref. 91 and the work on Co/Cu nanowires[57] and Co/Ag CPP-GMR multilayers.[56]

X. CONCLUSIONS

We have demonstrated spin injection and accumulation in metallic mesoscopic spin valves with transparent contacts. We have shown that in a conventional measurement geometry the magnetoresistance effects of the injecting and detecting contacts can be much larger than the spin valve effect, making it impossible to observe the spin valve effect in a conventional measurement geometry. However, these contact effects can be used to monitor the magnetization reversal

process of the spin injecting and detecting contacts. In a nonlocal measurement geometry we can completely isolate the spin valve effect, as was reported earlier in Ref. 19. Using this geometry we find spin relaxation lengths in Cu of around 1 μm at $T=4.2$ K and 350 nm at RT and spin relaxation lengths in Al of around 1.2 μm at $T=4.2$ K and 600 nm at RT. The associated spin relaxation times in Al and Cu are in good agreement with theory and values from experiments previously reported in the literature. The spin relaxation lengths in the Al and Cu thin films at RT are limited by electron-phonon scattering to a maximum length of about 1.2 μm and 600 nm, respectively. For Py we find spin relaxation lengths and current polarizations in agreement with CPP-GMR experiments. However, for Co we obtain values of $\alpha_F\lambda_F$ which are up to a factor of 20 smaller than their CPP-GMR counterpart. For Ni electrodes we are unable to resolve a spin valve signal within the limits of our experimental accuracy, corresponding with $\alpha_F\lambda_F$ at least a factor of 10 lower than expected. Finally, the use of tunnel barriers should make it possible to increase the polarization of the injected current in nonmagnetic metals, as we recently have shown.[21,22] This should make it possible to increase the spin signals to about 1 Ω in metals.

ACKNOWLEDGMENTS

The authors wish to thank H. Boeve, J. Das, and J. de Boeck at IMEC (Belgium) for support in sample fabrication, J. Fabian for making his material on spin relaxation times available to us, and the Stichting Fundamenteel Onderzoek der Materie for financial support.

*Electronic address: jedema@phys.rug.nl

†Present address: Department of Applied Physics and Center for Nanomaterials, Eindhoven University of Technology, 5600 MB, The Netherlands.

[1] *Semiconductor Spintronics and Quantum Computation*, edited by D. D. Awschalom, D. Loss and N. Samarth (Springer-Verlag, Berlin, 2002).

[2] G. A. Prinz, Science **282**, 1660 (1998).

[3] S. A. Wolf, D. D. Awschalom, R. A. Buhrmann, J. M. Daughton, S. von Molnár, M. L. Roukes, A. Y. Chtchelkanova, and D. M. Treger, Science **294**, 1488 (2001).

[4] M. A. M. Gijs and G. E. W. Bauer, Adv. Phys. **46**, 285 (1997).

[5] J-Ph. Ansermet, J. Phys.: Condens. Matter **10**, 6027 (1998).

[6] J. Bass and W. P. Pratt, Jr., J. Magn. Magn. Mater. **200**, 274 (1999).

[7] R. Meservey and P. M. Tedrow, Phys. Rep. **238**, 173 (1994).

[8] J. S. Moodera, L. R. Kinder, T. M. Wong, and R. Meservey, Phys. Rev. Lett. **74**, 3273 (1995).

[9] D. J. Monsma, R. Vlutters, and J. C. Lodder, Science **281**, 407 (1998); D. J. Monsma, J. C. Lodder, Th. J. A. Popma, and D. Dieny, Phys. Rev. Lett. **74**, 5260 (1995).

[10] W. H. Rippard and R. A. Buhrmann, Phys. Rev. Lett. **84**, 971 (2000).

[11] J. C. Slonczewski, J. Magn. Magn. Mater. **159**, L1 (1996).

[12] J. Z. Sun, Phys. Rev. B **62**, 570 (2000).

[13] J.-E. Wegrowe, D. Kelly, Y. Jaccard, Ph. Guittienne, and J.-Ph. Ansermet, Europhys. Lett. **45**, 626 (1999).

[14] E. B. Myers, D. C. Ralph, J. A. Katine, R. N. Louie, and R. A. Buhrmann, Science **285**, 867 (1999); J. A. Katine, F. J. Albert, R. A. Buhrman, E. B. Myers, and D. C. Ralph, Phys. Rev. Lett. **84**, 3149 (2000).

[15] J. Grollier, V. Cros, A. Hamzic, J. M. George, H. Jaffrès, A. Fert, G. Faini, J. Ben Youssef, and H. Legall, Appl. Phys. Lett. **78**, 3663 (2001).

[16] F. J. Jedema, Ph.D. thesis, Rijksuniversiteit Groningen, 2002.

[17] M. Johnson and R. H. Silsbee, Phys. Rev. Lett. **55**, 1790 (1985).

[18] M. Johnson and R. H. Silsbee, Phys. Rev. B **37**, 5312 (1988); Phys. Rev. B **37**, 5326 (1988).

[19] F. J. Jedema, A. T. Filip, and B. J. van Wees, Nature (London) **410**, 345 (2001).

[20] F. J. Jedema, M. S. Nijboer, A. T. Filip, and B. J. van Wees, J. Supercond. **15**, 27 (2002).

[21] F. J. Jedema, H. B. Heersche, A. T. Filip, J. J. A. Baselmans, and B. J. van Wees, Nature (London) **416**, 713 (2002).

[22] F. J. Jedema, M. V. Costache, H. B. Heersche, J. J. A. Baselmans, and B. J. van Wees, Appl. Phys. Lett. **81**, 5162 (2002).

[23] J. A. Caballero, C. E. Moreau, W. P. Pratt, Jr., and N. O. Birge, IEEE Trans. Magn. **37**, 2111 (2001).

[24] G. Schmidt, D. Ferrand, L. W. Molenkamp, A. T. Filip, and B. J. van Wees, Phys. Rev. B **62**, R4790 (2000).

[25] S. Datta, *Electronic Transport in Mesoscopic Systems* (Cambridge University Press, Cambridge, England, 1995).

[26] N. F. Mott, Proc. R. Soc. London, Ser. A **153**, 699 (1936); **156**, 368 (1936); Adv. Phys. **13**, 325 (1964).

[27] I. A. Campbell, A. Fert, and A. R. Pomeroy, Philos. Mag. **15**, 977 (1967).

[28] A. Fert and I. A. Campbell, J. Phys. (Paris), Colloq. **32**, C1-46 (1971).

[29] A. Fert and I. A. Campbell, J. Phys. F: Met. Phys. **6**, 849 (1976).

[30] I. A. Campbell and A. Fert, in *Ferromagnetic Materials*, edited by E. P. Wohlfarth (North-Holland, Amsterdam, 1982), Chap. 9, p. 747.

[31] P. C. van Son, H. van Kempen, and P. Wyder, Phys. Rev. Lett. **58**, 2271 (1987).

[32] T. Valet and A. Fert, Phys. Rev. B **48**, 7099 (1993).

[33] M. Johnson and R. H. Silsbee, Phys. Rev. B **35**, 4959 (1987).

[34] M. Johnson, Phys. Rev. Lett. **70**, 2142 (1993); Science **260**, 320 (1993).

[35] M. Johnson, J. Appl. Phys. **75**, 6714 (1994).

[36] A. Fert and S. Lee, Phys. Rev. B **53**, 6554 (1996).

[37] S. Hershfield and L. Z. Zhao, Phys. Rev. B **56**, 3296 (1997).

[38] M. B. Stears, J. Magn. Magn. Mater. **5**, 167 (1977).

[39] I. I. Oleinik, E. Yu. Tsymbal, and D. G. Pettifor, Phys. Rev. B **62**, 3952 (2000).

[40] S. Dubois, L. Piraux, J. M. George, K. Ounadjela, J. L. Duvail, and A. Fert, Phys. Rev. B **60**, 477 (1999).

[41] S. D. Steenwyk, S. Y. Hsu, R. Loloee, J. Bass, and W. P. Pratt, Jr., J. Magn. Magn. Mater. **170**, L1 (1997).

[42] P. Holody, W. C. Chiang, R. Loloee, J. Bass, W. P. Pratt, Jr., and P. A. Schroeder, Phys. Rev. B **58**, 12 230 (1998).

[43] A. Fert, J. L. Duvail, and T. Valet, Phys. Rev. B **52**, 6513 (1995).

[44] In our definition τ_{sf} is equal to the spin lattice relaxation time T_1 as used in the Bloch equations (Ref. 18) In the Valet-Fert (VF) theory $(\tau_{sf})^{VF}$ is different. The difference originates from a different expression for λ_{sf}^2. In the VF theory (Ref. 32) $\lambda_{sf}^2 = (1/D_\uparrow + 1/D\downarrow)^{-1}\tau_{sf}^{VF}$, whereas we derive $\lambda_{sf}^2 = [N_\downarrow/D_\uparrow(N_\uparrow + N_\downarrow) + N_\uparrow/D_\downarrow(N_\uparrow + N_\downarrow)]^{-1}\tau_{sf}$. In nonmagnetic metals the definition of Ref. 32] corresponds therefore to twice the value of our τ_{sf}: $(\tau_{sf})^{VF} = 2\tau_{sf} = 2T_1$.

[45] A. T. Filip, B. H. Hoving, F. J. Jedema, B. J. van Wees, B. Dutta, and S. Borghs, Phys. Rev. B **62**, 9996 (2000).

[46] S. F. Lee, W. P. Pratt, Jr., R. Loloee, P. A. Schroeder, and J. Bass, Phys. Rev. B **46**, 548 (1992).

[47] K. Hong and N. Giordano, Phys. Rev. B **51**, 9855 (1995).

[48] F. G. Monzon and M. L. Roukes, J. Magn. Magn. Mater. **198**, 632 (1999).

[49] J. Nitta, T. Schäpers, H. B. Heersche, T. Koga, Y. Sato, and H. Takayanagi, Jpn. J. Appl. Phys., Part 1 **41**, 2497 (2002).

[50] Th. G. S. M. Rijks, R. Coehoorn, M. J. M. de Jong, and W. J. M. de Jonge, Phys. Rev. B **51**, 283 (1995).

[51] Q. Yang, P. Holody, S.-F. Lee, L. L. Henry, R. Loloee, P. A. Schroeder, W. P. Pratt, Jr., and J. Bass, Phys. Rev. Lett. **72**, 3274 (1994).

[52] Q. Yang, P. Holody, R. Loloee, L. L. Henry, W. P. Pratt, Jr., P. A. Schroeder, and J. Bass, Phys. Rev. B **51**, 3226 (1995).

[53] M. Johnson, Nature (London) **416**, 809 (2002).

[54] M. Johnson, Semicond. Sci. Technol. **17**, 298 (2002).

[55] C. Vouille, A. Barthélémy, F. Elokan Mpondo, A. Fert, P. A. Schroeder, S. Y. Hsu, A. Reilly, and R. Loloee, Phys. Rev. B **60**, 6710 (1999).

[56] S.-F. Lee, Q. Yang, P. Holody, R. Loloee, J. H. Hetherington, S. Mahmood, B. Ikegami, K. Vigen, L. L. Henry, P. A. Schoeder, W. P. Pratt, Jr., and J. Bass, Phys. Rev. B **52**, 15 426 (1995).

[57] L. Piraux, S. Dubois, A. Fert, and L. Beliard, Eur. Phys. J. B **4**, 413 (1998); L. Piraux, S. Dubois, C. Marchal, J.M. Beuken, L. Filipozzi, J. F. Despres, K. Ounadjela, and A. Fert, J. Magn. Magn. Mater. **156**, 317 (1996).

[58] B. Doudin, A. Blondel, and J.-Ph. Ansermet, J. Appl. Phys. **79**, 6090 (1996).

[59] U. Ebels, A. Radulescu, Y. Henry, L. Piraux, and K. Ounadjela, Phys. Rev. Lett. **84**, 983 (2000).

[60] H. Kubota, M. Sato, and T. Miyazaki, Phys. Rev. B **52**, 343 (1995).

[61] W. P. Pratt, Jr., S.-F. Lee, J. M. Slaughter, R. Loloee, P. A. Schroeder, and J. Bass, Phys. Rev. Lett. **66**, 3060 (1991).

[62] C. Kittel, *Introduction to Solid State Physics*, 7th ed. (Wiley, New York, 1996).

[63] G. Bergmann, Phys. Rep. **107**, 1 (1984).

[64] Y. Yafet, in *Solid State Physics*, edited by F. Seitz and D. Turnbull (Academic, New York, 1963), Vol. 14.

[65] J. A. X. Alexander, P. M. Tedrow, and T. P. Orlando, Phys. Rev. B **34**, 8157 (1986).

[66] P. Fulde, Adv. Phys. **22**, 667 (1973).

[67] R. J. Elliot, Phys. Rev. **96**, 266 (1954).

[68] J. Fabian and S. Das Sarma, J. Vac. Sci. Technol. B **17**, 1708 (1999).

[69] P. Monod and F. Beuneu, Phys. Rev. B **19**, 911 (1979).

[70] J. Bass, in *Metals: Electronic Transport Phenomena*, edited by K. H. Hellwege and J. L. Olsen, Landolt-Börnstein, New Series, Group 3, Vol. 15, Part a (Springer-Verlag, Berlin, 1982).

[71] F. Beuneu and P. Monod, Phys. Rev. B **18**, 2422 (1978).

[72] D. Lubzens and S. Schultz, Phys. Rev. Lett. **36**, 1104 (1976).

[73] S. Schultz and C. Latham, Phys. Rev. Lett. **15**, 148 (1965).

[74] F. Beuneu and P. Monod, Phys. Rev. B **13**, 3424 (1976).

[75] P. Monod and A. Janossy, J. Low Temp. Phys. **26**, 311 (1977).

[76] J. Fabian and S. Das Sarma, Phys. Rev. Lett. **81**, 5624 (1998).

[77] J. Fabian and S. Das Sarma, J. Appl. Phys. **85**, 5075 (1999).

[78] J. Fabian and S. Das Sarma, Phys. Rev. Lett. **83**, 1211 (1999).

[79] N. W. Ahscroft and N. D. Mermin, *Solid State Physics* (Saunders, Orlando, FL, 1976).

[80] D. A. Papaconstantopoulos, *Handbook of the Band Structure of Elemental Solids* (Plenum, New York, 1986).

[81] G. Bergmann, Phys. Rev. B **29**, 6114 (1984).

[82] J. M. Gordon, C. J. Lobb, and M. Tinkham, Phys. Rev. B **28**, R4046 (1983).

[83] R. Meservey, P. M. Tedrow, and R. C. Bruno, Phys. Rev. B **11**, 4224 (1975).

[84] C. Grimaldi and P. Fulde, Phys. Rev. Lett. **77**, 2550 (1996).

[85] D. J. Monsma and S. S. P. Parkin, Appl. Phys. Lett. **77**, 720 (2000).

[86] J. R. Petta and D. C. Ralph, Phys. Rev. Lett. **87**, 266801 (2001).

[87] P. Monod and S. Schultz, J. Phys. (Paris) **43**, 393 (1982).

[88] P. M. Levy, Solid State Phys. **47**, 367 (1994).

[89] K. M. Schep, J. B. A. N. van Hoof, P. J. Kelly, G. E. W. Bauer, and J. E. Inglesfield, Phys. Rev. B **56**, 10 805 (1997); see also K. Schep, Ph.D. thesis, Delft University of Technology, 1997.

[90] K. Xia, P. J. Kelly, G. E. W. Bauer, I. Turek, J. Kudrnovsky, and V. Drchal, Phys. Rev. B **63**, 064407 (2001).

[91] E. Yu. Tsymbal and D.G. Pettifor, Phys. Rev. B **54**, 15 314 (1996).

[92] W. Park, D. V. Baxter, S. Steenwyk, I. Moraru, W. P. Pratt, Jr., and J. Bass, Phys. Rev. B **62**, 1178 (2000).

[93] C. H. Marrows and B. J. Hickey, Phys. Rev. B **63**, 220405 (2001).

[94] W. F. Egelhoff, Jr. and P. J. Chen, C. J. Powell, M. D. Stiles, R. D. McMichael, C.-L. Lin, J. M. Sivertsen, J. H. Judy, K. Takano, A. E. Berkowitz, T. C. Anthony, and J. A. Brug, J. Appl. Phys. **79**, 5277 (1996).